Post-perihelion mapping of wind-tail-like features on comet 67P/Churyumov-Gerasimenko using remote sensing imagery of ESA's Rosetta mission

72 Pages with 44 Figures, 4 Tables, 1 Appendix

submitted as BSc Thesis

at the Institute for Geosciences
of the Rheinische Friedrich-Wilhelms University of Bonn

in association with
the DLR Institute of Planetary Research in Berlin

by Jan R. Burkhardt

1. Supervisor: PD Dr. Katharina A. Otto

2. Supervisor: Prof. Dr. Tom McCann

Bonn, August 2024

Eidesstattliche Erklärung

Hiermit erkläre ich, dass ich die vorliegende Arbeit selbstständig verfasst und keine anderen als die angegebenen Quellen und Hilfsmittel verwendet habe.

Bonn, 11.08.2024, Jan Luca Burkhardt

Ort, Datum, Unterschrift

Dedication

In remembrance to my grandfather Ewald. Together, we visited that odd even older man (who was probably family too), when I was a kid. His hobby was locating the ISS from his 'office', which really needed a clean-up. For young Jan, it was quite strange, as it looked like this guy was somehow trying to communicate with outer space using his pimped-up toaster. At least I can appreciate it now. Grandpa, thank you for everything.

Contents

1 Introduction **1**

1.1 Aeolian Wind Tails 2

1.2 Motivation & Objectives 4

2 Comets **5**

2.1 Comet 67P/Churyumov-Gerasimenko 9

2.2 Cometary Activity of Comet 67P 11

3 Geological Diversity of Comet 67P **13**

3.1 Exposed Consolidated Surfaces 15

3.2 Large-scale Depression Structures 16

3.3 Brittle Material with Pits & Circular Structures 17

3.4 Non-Consolidated Material with Wind-Tail-like Features 18

4 Material and Methods **25**

4.1 Data 26

4.2 Image Categorisation Process & Classification Scheme 29

4.3 Performing Measurements with the SBMT 33

4.4 Projecting the Results in Paraview 37

5 Results **38**

6 Discussion **42**

6.1 Distribution of Wind-Tail-like Features 42

6.2 Morphological Types of Wind-Tail-like Features 43

6.3 Orientations of Wind-Tail-like Features 45

6.4 Pre- and Post-Perihelion Comparison 46

7 Conclusion **54**

8 Acknowledgements **55**

9 References **56**

List of Figures

1 Rosetta's journey from 2004 to 2016 (Image Credit: ESA). 1

2 Aoelian wind tails on Earth, in the Grand Falls Dune Field, Arizona, USA. Material has accumulated in a wedge-shaped, elongated form behind an obstacle (vegetation), the wind direction is highlighted by a blue arrow (from Sachse *et al.* 2021). 2

3 Terminology of wind-tail-like features presented in a sketch, with a boulder functioning as an obstacle, the wind direction is indicated by a blue arrow. 3

4 (a) Long-period comet C/1995 O1, called Hale-Bopp. Showing a coma which hides the comet's nucleus inside, and an ion tail (blue) as well as a dust tail (yellow). (b) Short-period comet 67P, showing only a dust tail (from Rossi & van Gasselt 2018). 5

5 Comet Hale-Bopp with an ion tail and a dust tail (from Bennett *et al.* 2020). 6

6 Changes of a comet during its orbit (from Bennett *et al.* 2020). 7

7 Illustration showing the main repositories of comets in the Solar System, the Oort Cloud and the Kuiper Belt (Source: ESA). 8

8 True color image of comet 67P taken by the Rosetta spacecraft's OSIRIS Narrow Angle Camera on 17 March 2015, calculated with a four frame mosaic, each color frame imaged through VIS-BLUE, VIS-GREEN, and VIS-RED filters, distance roughly 82 km from the comet's center (Image Credit: ESA). 9

9 Image rendered in false colors, taken on 15 April 2015, showing the comet's activity due to sublimation-driven outgassing (Image Credit: ESA). 10

10 Active pit in the Seth region, distance to the comet 60 km. On the right with enhanced contrast, the fine structures in the pit's shadow are interpreted as jets due to sublimation-driven outgassing (from Sierks *et al.* 2015). 11

11 (A & B) Outburst of cometary activity in the Imhotep region (B is a zoomed-in version of A). (C) The same area before (2 May 2016) and (D) after the event (24 July 2016), leaving behind an ice patch of c. 10 m in size (white arrow) (from El-Maarry *et al.* 2019). 12
12 Geological regions of 67P's northern hemisphere (from Thomas *et al.* 2015a). 13
13 Exposed consolidated surface in the Hathor region, which appears rocky and robust, with horizontal and vertical lineaments (from Thomas *et al.* 2015a). 15
14 Above and side view of the Hatmehit region (from La Forgia *et al.* 2015). 16
15 Circular pit (indicated with an A) in the Seth region with brittle material that forms talus- and rockfall-like deposits, visible especially in the image's bottom left quadrant (from El-Maarry *et al.* 2015). 17
16 Terrains in the northern hemisphere of comet 67P, NCM stands for 'non-consolidated material', ECS is 'exposed consolidated surface' (El-Maarry *et al.* 2019). 18
17 Close-up view of two sites in the Imhotep region, showing fine material that forms the smooth terrains (from Auger *et al.* 2015). At the edges it looks like the NCM airfall deposits are layered (Thomas *et al.* 2015a). 19
18 Dune-like structures observed in the Ma'at and Hatmetit regions of comet 67P (from La Forgia *et al.* 2015). 20
19 Gravitational inclines in the Imhotep region with the borders of smooth deposits, and boulders shown in red (from Auger *et al.* 2015). The yellow square shows the image area shown in Figure 43. 21
20 (Left): Aeolian-like ripple field in the Hapi region. (Right): Lateral view of the ripples (red arrow) (from Thomas *et al.* 2015b). 22
21 Scheme of the proposed airfall-driven depositional process, producing the ripple-like structures in the Hapi region, and the widely distributed NCM layer on the surface of comet 67P (after Thomas *et al.* 2015b). . 22
22 Example of three wind-tail-like features in 67P's Hapi region. 23
23 Material transport mechanisms in (a) aeolian, (b) subaqueous, and (c) cometary environments (from Jia *et al.* 2017). 24

24 Simulation results reproducing the basic morphology of the observed wind-tail-like features on comet 67P, suggesting the erosional rather than depositional nature (after Mottola *et al.* 2015). 24
25 Main tasks in conducting the analysis of this BSc thesis. 25
26 Changes in distance between the Rosetta Orbiter and the centre of comet 67P in the period from December 2014 to July 2016 (from Taylor *et al.* 2017), the perihelion took place on 13 August 2015 (Barrington *et al.* 2023), the observation period used for this BSc thesis is highlighted with a yellow square. 27
27 Flowchart of the image categorisation process. 29
28 Examples for wind-tail-like features 'type A'. 1a/2a: Original image, 2a/2b: Same image but with yellow lines indicating the length of the wind-tail-like features and blue lines showing the length and width of the boulder. 'Type A' characteristics are (i) material accumulated in a streamlined elongate shape pointing in a predominant direction (which may also be curved), (ii) the length of the wedge is greater than the length and width of the boulder, (iii) the shape is a closed form that is pointed at one end (i.e. the end extending away from the boulder), and (iv) the wedge has a ridge (which can be sharp or rounded). 31
29 Examples for wind-tail-like features 'type B'. 1a/2a: Original image, 2a/2b: Same image but with yellow lines indicating the length of the wind-tail-like features and blue lines showing the length and width of the boulder. 'Type B' characteristics are (i) accumulated material does not spread out to form a wide elongated shape, (ii) the entire wind tail is not extended further, than by a factor of 1, of the height and width of the boulder, (iii) the wind tail morphology fades out away from the boulder (i.e. it becomes narrower, but there is no identifiable end point), and (iv) the wedge does not necessarily need to have a ridge (but may have one). 32

30 Example of a projected image on shape model 'DLR SHAP4S' by Preusker *et al.* 2015 in the neck-region of comet 67P/Churyumov-Gerasimenko, produced with the SBMT. The position of the orbiter at the moment the image was captured is highlighted by green lines. The edges of the image are marked in red. The space probe is not accurate neighter in scale nor in orientation. 33
31 Illustration of the facet on which the wind-tail-like feature and boulder are located. The height of the boulder was estimated as half the mean value of the boulder's width and length, here labeled boulder size (from Otto *et al.* 2017). 35
32 Example image section showing the measured parameters in SBMT (yellow: length of the wind-tail-like feature, blue: boulder dimensions, red: the shape model's plate). Bottom: Equivalent image section with the texture of the shape model, so that the plate on which the boulder is located could be measured. 36
33 Post-perihelion findings of wind-tail-like features on comet 67P, categorised in 27 type A (orange) and 43 type B (blue) ('front' view). All findings on the 'back', as shown in Figure 35, were categorised as type B. Green lines indicate the boundaries of geological regions. 38
34 Post-perihelion 3D overview map of the distribution and orientation of wind-tail-like features on the surface of the northern hemisphere of comet 67P ('front' view). The arrows are coloured according to their length. Green lines indicate the boundaries of geological regions. 39
35 Post-perihelion 3D overview map of the distribution and orientation of wind-tail-like features on the surface of the northern hemisphere of comet 67P ('back' view of the 'body' lobe). The arrows are coloured according to their length. Green lines indicate the boundaries of geological regions. 39
36 Plot of the boulder sizes (mean of the boulder's length and width) and the lengths of the wind-tail-like features, in the observation period from 01 May to 31 July 2016 (post-perihelion) with 70 features identified (linear slope fit of 1.04). 40

37 Plot of the boulder sizes (mean of the boulder's length and width) and the lengths of the wind-tail-like features, in the observation period from 01 May to 31 July 2016 (post-perihelion), categorised in 27 type A (orange) and 43 type B (blue). 40
38 Plot of the boulder sizes (mean of the boulder's length and width) and the lengths of the wind-tail-like features. Pre-perihelion findings according to Sachse *et al.* (2022) (yellow), 39 features, slope fit 0.94. Post-perihelion results of this BSc thesis (green), 70 features, slope fit 1.04. . 47
39 Plot of the boulder sizes (mean of the boulder's length and width) and the lengths of the wind-tail-like features. Pre-perihelion findings according to Sachse *et al.* (2022) (yellow), 39 features, slope fit 0.94. Post-perihelion, categorised in 27 type A (orange) and 43 type B (blue). Slope fits: 0.85 (type A), 0.69 (type B). 47
40 Pre-perihelion 3D overview map of the distribution and orientation of wind-tail-like features on the surface of the northern hemisphere of comet 67P ('front' view). Data from Sachse *et al.* (2022). The arrows are coloured according to their length. Green lines indicate the boundaries of geological regions. 48
41 Pre-perihelion 3D overview map of the distribution and orientation of wind-tail-like features on the surface of the northern hemisphere of comet 67P ('back' view of the 'body' lobe). Data from Sachse *et al.* (2022). The arrows are coloured according to their length. Green lines indicate the boundaries of geological regions. 48
42 Comparison in the Hapi 'neck' region, small letters indicate the corresponding boulders. (Top): Pre-perihelion image from 22 January 2015. (Bottom): Post-perihelion measurements of this BSc thesis, image taken on 19 June 2016. 51

43 Comparison in the Imhotep region, on the 'back' of the 'body' lobe. The numbers as well as small letters indicate the corresponding boulders in the different images. 1-3 with green lines show possible mass wasting deposits 'before' boulders. The letters a-c with yellow lines indicate possible wind-tail-like features. In these images, all wind-tail-like features are categorised as type B. (Top): Pre-perihelion image from 14 February 2015. (Bottom): Post-perihelion measurements of this BSc thesis, image taken on 14 June 2016. 52

44 Example images of different perspectives on the same area, here within the Serqet region. (Top): Pre-perihelion (from Tirsch *et al.* 2017). (Bottom): Post-perihelion (this BSc thesis). 53

List of Tables

1 Tabular overview of the northern hemisphere's geological regions on comet 67P/Churyumov-Gerasimenko (abbreviated representation from El-Maarry *et al.* 2015). 'B': body lobe, 'N': neck region, 'H': head lobe. Categories based on Thomas *et al.* 2015a: (1) Exposed consolidated surfaces, (2) large-scale depressions, (3) brittle materials with pits and circular structures, as well as (4) dust-covered terrains, and (5) smooth terrains (both are NCM airfall deposits). 'X' means that the feature occurs, 'X*' indicates that it is the dominant feature of the region. . . . 14

2 Parameters set as filter settings for narrowing the search in ESA's PSA. 26

3 Data comparison table of the pre-perihelion results (Sachse *et al.* 2022) with the post-perihelion measurements (of this given BSc thesis), showing average values. 46

4 Table of the images used for the measurements in the SBMT. ALTITUDE describes the spacecraft's distance to the comet's surface. For NAC-images: RESOLUTION = 0.00001875 * ALTITUDE. 61

1 Introduction

Beginning this given BSc thesis, a brief overview of ESA's Rosetta mission is provided. Subsequently, aeolian wind tails are introduced, which commonly occur on planets such as Earth and Mars (also see Section 1.1). Afterwards, the motivation and the objectives of this study are outlined (also see Section 1.2).

The European Space Agency's Rosetta mission launched from Earth on 2 March 2004 (Figure 1). Originally, the mission was planned to visit comet 46P/Wirtanen, but due to issues with the launcher and further delay, comet 67P was selected as the new target (Taylor *et al.* 2017). After a ten year journey with flybys of Earth, Mars, and the asteroids 21 Lutetia and 2867 Šteins, the Rosetta spacecraft rendezvued with comet 67P/Churyumov–Gerasimenko (hereafter 67P) on 6 August 2014 (Thomas *et al.* 2015b). Rosetta's lander Philae became the first spacecraft on a comet nucleus on 12 November 2014 (Figure 1). On 30 September 2016, the Rosetta spacecraft ended its mission by way of a controlled impact on the comet's surface (Taylor *et al.* 2017), located in its Ma'at region (also see Section 2.1).

The main goals of ESA's Rosetta mission were to map comet 67P by remote sensing and to examine its environment in situ, as well as to investige its evolution within the inner Solar System (Taylor *et al.* 2017).

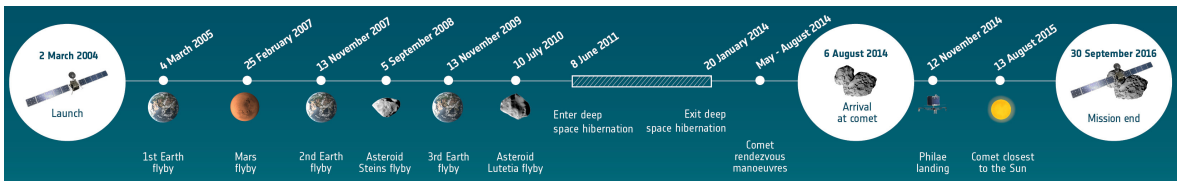

Figure 1: Rosetta's journey from 2004 to 2016 (Image Credit: ESA).

1.1 Aeolian Wind Tails

Aeolian wind tails are deposits of granular material that form as a result of accumulation or erosion behind an obstacle, and are indicating the wind direction (Sachse *et al.* 2022). They are commonly observed on planets with atmospheres, such as Earth and Mars (Figure 2), and consist of an elongated wedge with a ridge top. At the contact point, the accumulated material touches the obstacle, whereas at the tip, the wind tail's morphological appearance blends into the underlying sedimentary cover (Figure 3).

Figure 2: Aoelian wind tails on Earth, in the Grand Falls Dune Field, Arizona, USA. Material has accumulated in a wedge-shaped, elongated form behind an obstacle (vegetation), the wind direction is highlighted by a blue arrow (from Sachse *et al.* 2021).

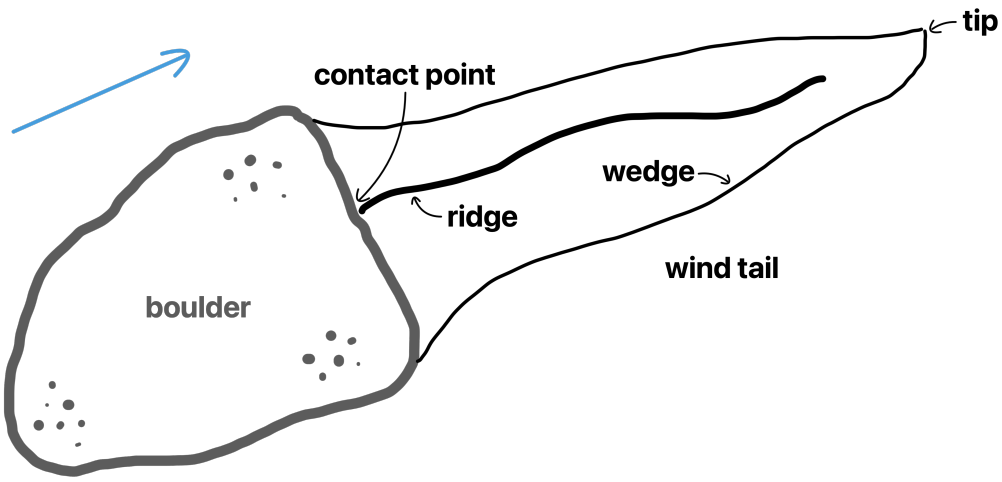

Figure 3: Terminology of wind-tail-like features presented in a sketch, with a boulder functioning as an obstacle, the wind direction is indicated by a blue arrow.

1.2 Motivation & Objectives

The existence of aeolian-like bedforms, including wind-tail-like features, on comet 67P, is striking given the almost negligible gravity and absence of a traditional atmosphere in the cometary environment. This motivates to verify and deepen the scientific knowledge of this research field with this present study.

The study of comets is of importance as these small bodies spend the majority of their existence at far distances from the Sun, allowing them to retain the most primordial elements of the Solar System, including volatiles such as water (also see Section 2). Furthermore, comets provide insights into the composition of the interstellar cloud from which our Sun and planets formed (Taylor *et al.* 2017). Understanding the phenomena on the comets surface, which includes the study of wind-tail-like features, has a significant impact for the overall comprehension of these small bodies, gaining more scientific knowledge about our Solar System, and our place within it.

Utilizing remote sensing images of ESA's Rosetta mission, it is the objective of this given BSc thesis to determine how wind-tail-like features behave on comet 67P. This includes the post-perihelion distribution of wind-tail-like features on the comet's surface, addressing the question whether there are areas that present more favourable conditions for their formation (also see Section 6.1). Furthermore, it is of particular interest to investigate whether new perspectives can be gained regarding the formation process of wind-tail-like features on comet 67P (also see Section 6.2), based on the classification of the two morphological types of wind-tail-like features introduced in this study (also see Section 4.2). Moreover, an analysis of the orientations of the wind-tail-like features on comet 67P will be conducted to examine whether conclusions can be drawn regarding the origin of the material that resulted in the formation of these structures (also see Section 6.3). All these post-perihelion findings will be compared with the results of previous studies, in particular Sachse *et al.* (2022), dealing with wind-tail-like features before comet 67P's perihelion transit (also see Section 6.4). It is worth noting that this comparison of pre- and post-perihelion of wind-tail-like structures on a comet had not previously been conducted, prior to the research presented in this given BSc thesis.

2 Comets

This Chapter provides a general overview about comets, before introducing comet 67P (also see Section 2.1). Additionally, the concept of cometary activity is explained (also see Section 2.2), as it is crucial for understanding how material on 67P's surface is brought into motion, which may result in the formation of aeolian-like structures, such as wind-tail-like features (also see Section 3.4).

Comets are classified according to their orbital period, which is either long- or short-period (Figure 4) with the basic terminology (Figure 5) comprising the comet's nucleus, a coma, and typically two tails, an ion tail as well as a dust tail (Rossi & van Gasselt 2018). Approaching the Sun, the volatile compounds (most dominantly H_2O, CO and CO_2) of the comet's nucleus start degassing (Figure 6). The coma is the visible part consisting of a bright cloud of gas and dust, which is surrounded by a wide hydrogen cloud, generated by the dissociation of H-bearing molecules under the effect of UV solar radiation (Rossi & van Gasselt 2018). The ion tail is generated by photodissociation and photoionization of the sublimating gas molecules emitted by the comet (Rossi & van Gasselt 2018), and points away radially from the Sun (Figure 6).

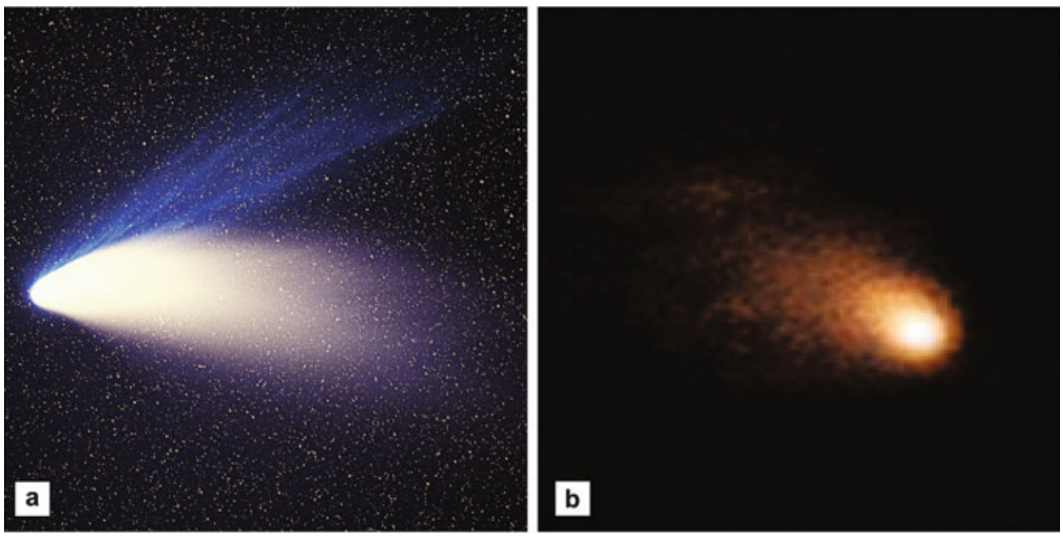

Figure 4: (a) Long-period comet C/1995 O1, called Hale-Bopp. Showing a coma which hides the comet's nucleus inside, and an ion tail (blue) as well as a dust tail (yellow). (b) Short-period comet 67P, showing only a dust tail (from Rossi & van Gasselt 2018).

In contrast to the ion tail, dust-particles that escape from the coma are not blown away by the solar wind, but are pushed away from the Sun by the much weaker pressure of the sunlight, which is called 'light radiation pressure' (Bennett *et al.* 2020). Dust tails are therefore slightly bent in the direction from which the comet came (Figures 5 and 6).

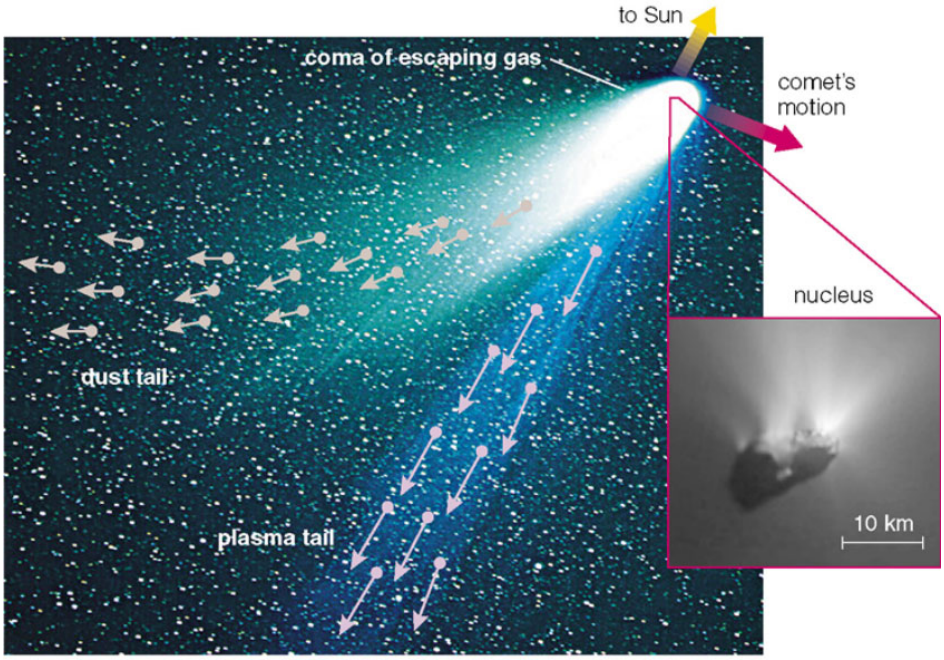

Figure 5: Comet Hale-Bopp with an ion tail and a dust tail (from Bennett *et al.* 2020).

Long-period comets, having spectacular comas and tails, are characterised by orbital periods commonly exceeding 200 years and extending to about 10 Ma, with highly variable orbital inclinations and aphelions (the furthest position away to the Sun) extending beyond the external planets of the Solar System (Rossi & van Gasselt 2018). The source of these comets is the Oort Cloud (Figure 7), a spherical reservoir of approximately up to 10^{13} small objects extending from 10^3 to 10^5 AU from the Sun (Bennett *et al.* 2020, Rossi & van Gasselt 2018). The relative motion of passing stars and giant molecular clouds in the interstellar medium can perturb objects in the Oort Cloud, ejecting them from the Solar System or reducing their perihelion (closest position to the Sun) distances to values that allow comas and tails to form, due to the closer distance to the Sun. Additionally, galactic tides, caused by the differential gravitational forces of stars and interstellar matter, can have similar effects ejecting long-period comets from the Oort Cloud (Rossi & van Gasselt 2018).

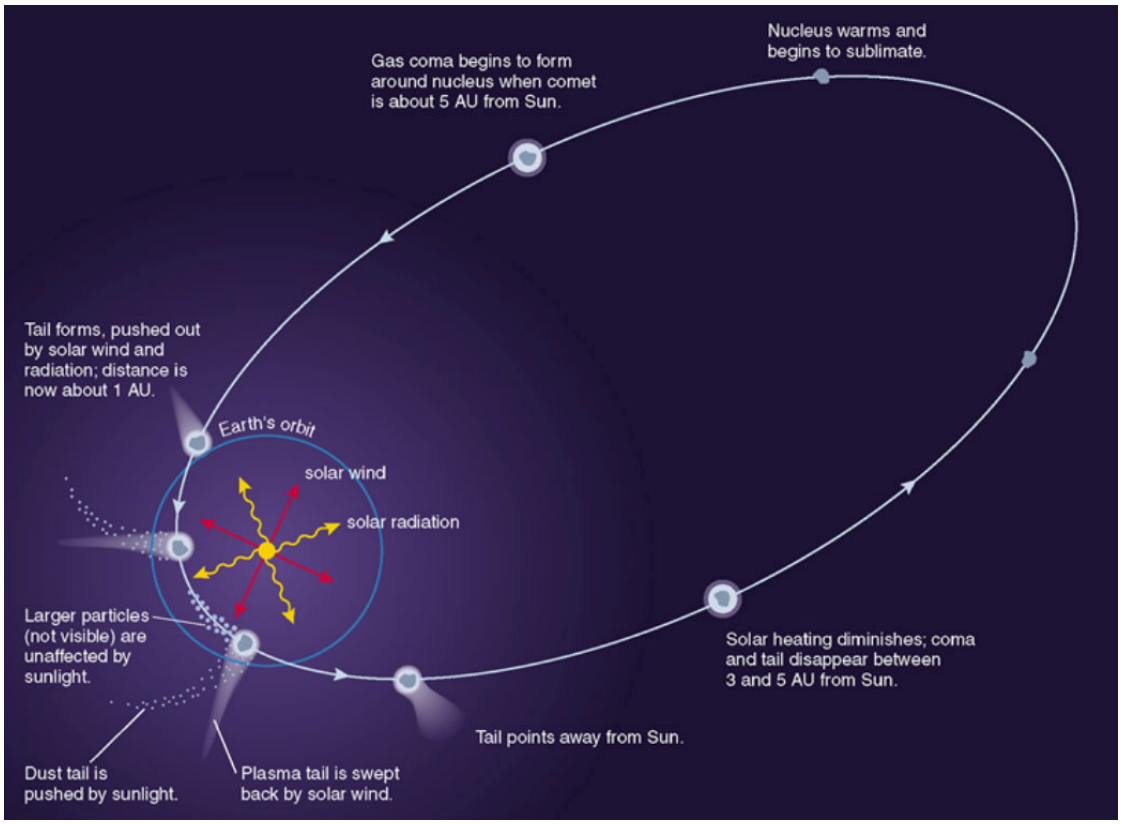

Figure 6: Changes of a comet during its orbit (from Bennett *et al.* 2020).

Short-period comets show less remarkable, weak comas and modest tails, which are often undetectable to the observation of the human eye (Rossi & van Gasselt 2018). Furthermore, they are characterised by their periodicity, which is shorter than 200 years, semi-major orbital axes less than 34 AU, and low orbital inclinations less than 35° (Rossi & van Gasselt 2018). Most are called Jupiter family comets having periods lower than 20 years, perihelion distances of one to a few AU, and aphelions in the Jupiter region (Bennett *et al.* 2020). The proposed reservoir for short-period comets, due to the low orbital inclination and shorter semi-major axis of these comets, is a belt extending beyond the orbit of Neptune (Rossi & van Gasselt 2018), which is called Kuiper Belt. This Scattered Disk extends from about 30 to 50 AU and holds about 10^{10} objects (Figure 7). Gravitational interactions with the giant planets (Neptune in particular), and collisions among the Kuiper Belt objects themselves convert these objects into short-period comets, which have weaker tails since the activity of the nucleus is often hampered by a mantle of refractory carbonaceous and silicate dust particles covering most of its surface, due to their more frequent perihelion transits compared to long-period comets (Rossi & van Gasselt 2018).

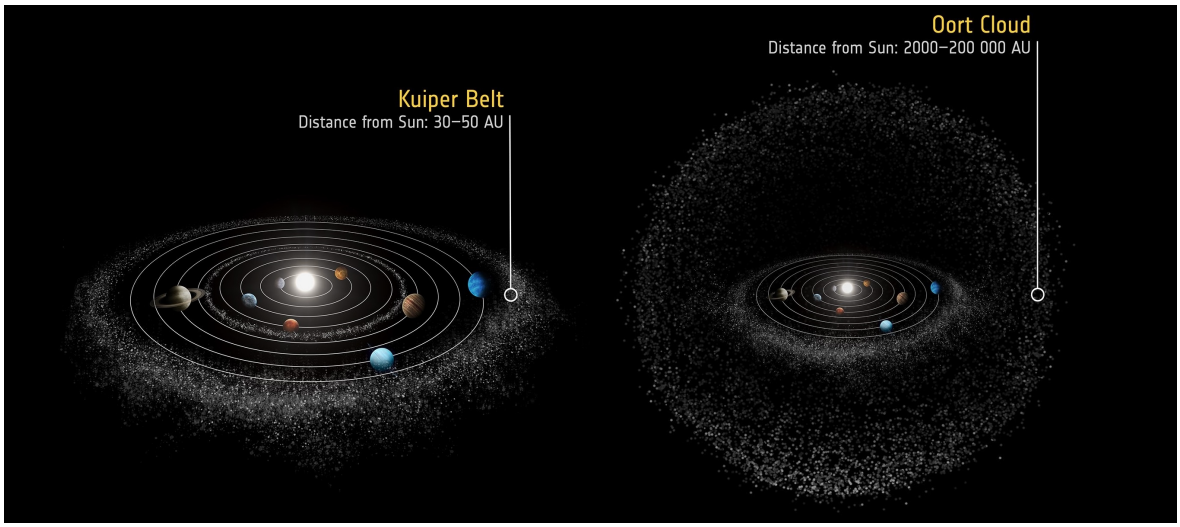

Figure 7: Illustration showing the main repositories of comets in the Solar System, the Oort Cloud and the Kuiper Belt (Source: ESA).

2.1 Comet 67P/Churyumov-Gerasimenko

Comet 67P has its origins in the Kuiper Belt, in the outer region of the solar system. Gravitational forces propelled it from this location bringing the comet into an orbit which crosses that of Jupiter, this is why 67P classifies as a Jupiter family comet (Rossi & van Gasselt 2018). Its furthest point from the Sun (aphelion) is located at a distance of 5.7 AU, whereas the perihelion of the comet, its closest point to the Sun, is positioned at 1.2 AU, which is between the orbits of Earth and Mars (Taylor *et al.* 2017).

Figure 8: True color image of comet 67P taken by the Rosetta spacecraft's OSIRIS Narrow Angle Camera on 17 March 2015, calculated with a four frame mosaic, each color frame imaged through VIS-BLUE, VIS-GREEN, and VIS-RED filters, distance roughly 82 km from the comet's center (Image Credit: ESA).

Comet 67P forms two lobes connected by a narrow 'neck region' (El-Maarry *et al.* 2015, also see Figure 8), which contains only 7% of the comet's volume. The entire comet's dimensions are determined c. 4.3 × 2.6 × 2.1 km. The larger 'body' lobe is 4.1 × 3.5 × 1.6 km in size, the smaller 'head' lobe is 2.5 × 2.1 × 1.6 km (Jorda *et al.*

2016). The Hapi 'neck' region's dimensions are 2.2 km × 0.8 km, which represents a partial loop of 140° around the comet's neck (Thomas *et al.* 2015a).

The total comet's volume is c. 18.6 km^3. The mean density of c. 537.8 kg/m^3 (less than water) was calculated (Preusker *et al.* 2017) based on the estimated mass of 9.98×10^{12} kg (Pätzold *et al.* 2016), and indicates a high porosity of the comet of 75% to 85% (Kofman *et al.* 2015). The albedo of the comet's surface is 0.06 (Capaccioni *et al.* 2015). Changes in the spin period of the comet were observed (in 2014: c. 12.404 hours; in May 2015: increase to c. 12.430 hours; in August 2015: drop to c. 12.305 hours), which means that the rotation speed increased over the lifespan of the Rosetta mission, caused by the comet's activity (Jorda *et al.* 2016).

67P's gravity is c. 10^{-5} times of that observed on Earth, and is nevertheless responsible for mass-wasting events on the comet's surface (El-Maarry *et al.* 2019). The comet is devoid of a traditional atmosphere. Instead, the comet's activity (also see Section 2.2), as a result of sublimation-driven outgassing through jets (Figure 9), forms a coma around the nucleus (El-Maarry *et al.* 2019), which develops a transient atmosphere that interacts with the surface by transporting materials (also see Section 3.4).

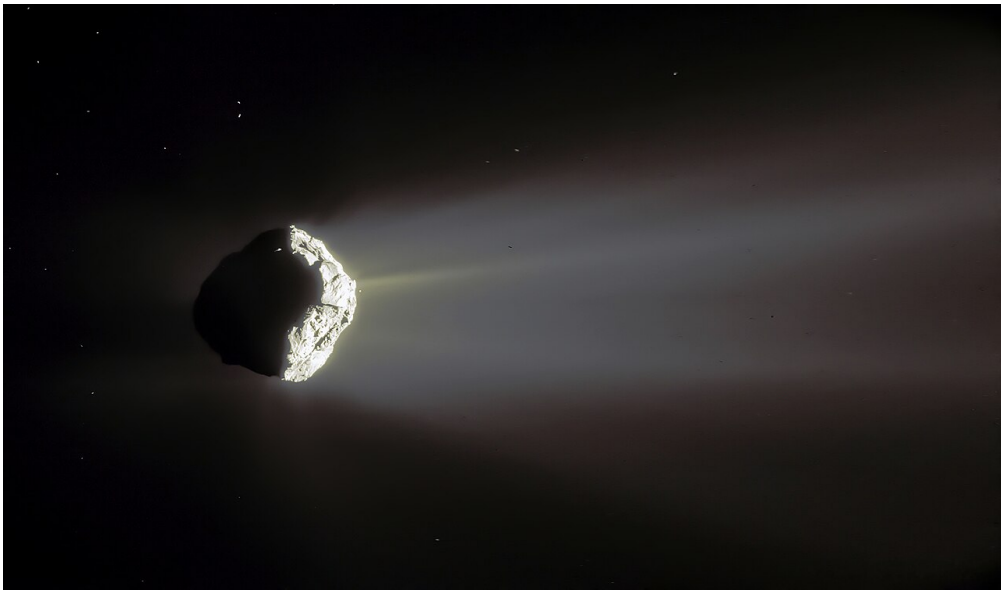

Figure 9: Image rendered in false colors, taken on 15 April 2015, showing the comet's activity due to sublimation-driven outgassing (Image Credit: ESA).

2.2 Cometary Activity of Comet 67P

Approaching the Sun, comets become active in the form of sublimation-driven outgassing (Figure 6). The scientific term for this is 'cometary activity' (El-Maarry *et al.* 2019). During this process, material gets ejected from the comet's nucleus by jets (Figure 10). These ejecta form a coma around the nucleus, when the comet is close enough to the Sun (El-Maarry *et al.* 2019). Cometary activity is mainly related to dust and not to ice particles (Thomas *et al.* 2015a). The process of cometary activity develops a transient atmosphere that interacts with the surface by transporting materials (El-Maarry *et al.* 2019). If the ejected particles do not reach the comet's escape velocity, resedimentation of these ejected material appears in the form of NCM airfall deposits (also see Section 3.4).

On comet 67P, several quasi-circular pits are minor sources of cometary activity (Figure 10). Thus, these pits presumably are erosion features (Sierks *et al.* 2015). Dust deposits similar to those in the Ash and Ma'at regions can be observed in inactive pits (Thomas *et al.* 2015a, also see Section 3.4), which are much shallower than the active ones. It has yet to be clarified, whether the pits are inactive or if they 'wake up', when getting illuminated more by the Sun (Sierks *et al.* 2015).

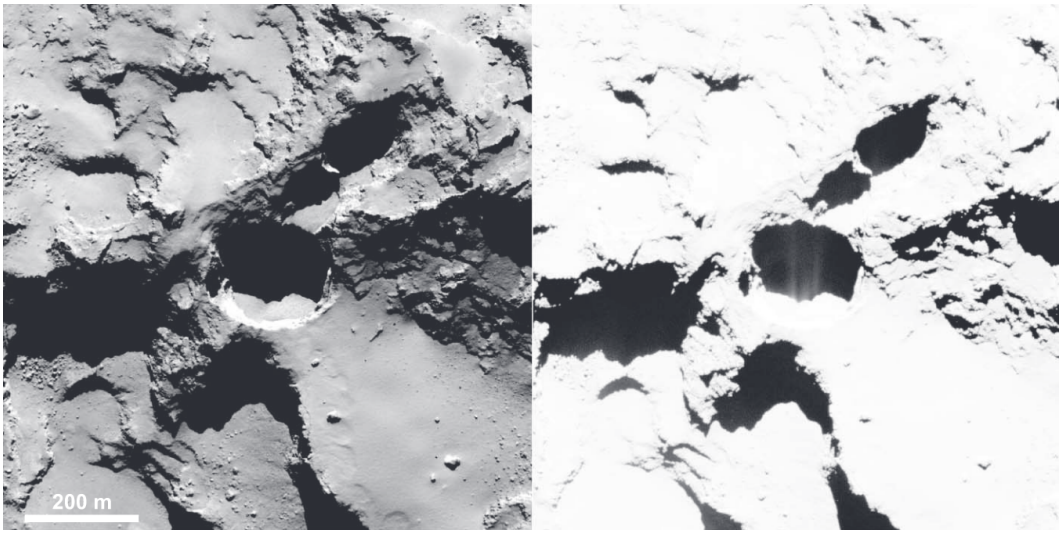

Figure 10: Active pit in the Seth region, distance to the comet 60 km. On the right with enhanced contrast, the fine structures in the pit's shadow are interpreted as jets due to sublimation-driven outgassing (from Sierks *et al.* 2015).

However, cometary activity has a depositional (in the form of resedimentation in airfall-like NCM deposits) and an erosive aspect. An outburst, observed on 3 July 2016 in the Imhotep region, left behind an ice patch c. 10 m ice in size (Figure 11), showing that these events can result in the erosion of surface materials and the exhumation of near-surface ice (El-Maarry *et al.* 2019).

It is assumed that chunks of ice or particles larger than a few millimetres ejected from the source do not sublimate before they fall to the surface (Thomas *et al.* 2015a).

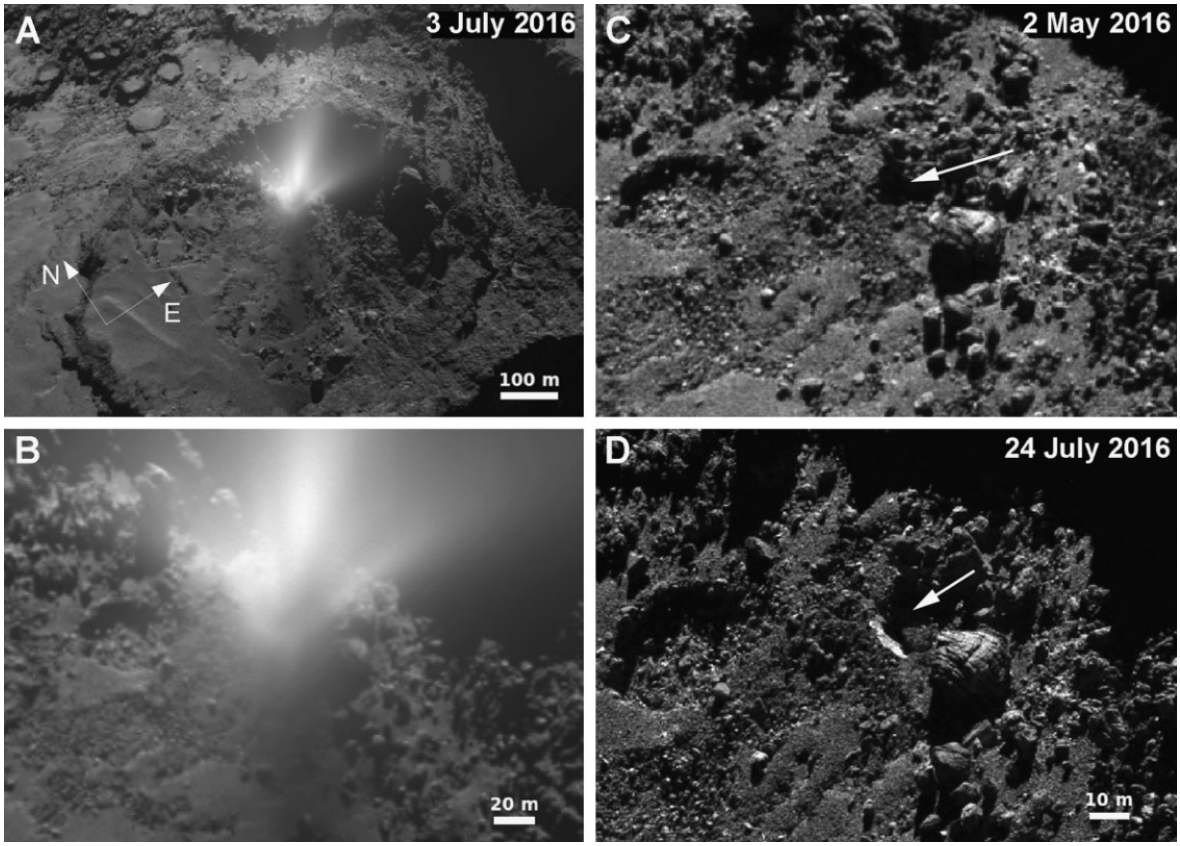

Figure 11: (A & B) Outburst of cometary activity in the Imhotep region (B is a zoomed-in version of A). (C) The same area before (2 May 2016) and (D) after the event (24 July 2016), leaving behind an ice patch of c. 10 m in size (white arrow) (from El-Maarry *et al.* 2019).

3 Geological Diversity of Comet 67P

For the northern hemisphere of the comet 67P (Figure 12), 19 geological regions have been defined due to morphological and/or structural boundaries (El-Maarry *et al.* 2015). The regions were named after Egyptian deities. After the comet's southern hemisphere was sufficiently illuminated by the Sun, seven more regions were discovered, bringing the total number of geological regions up to 26 (El-Maarry *et al.* 2016).

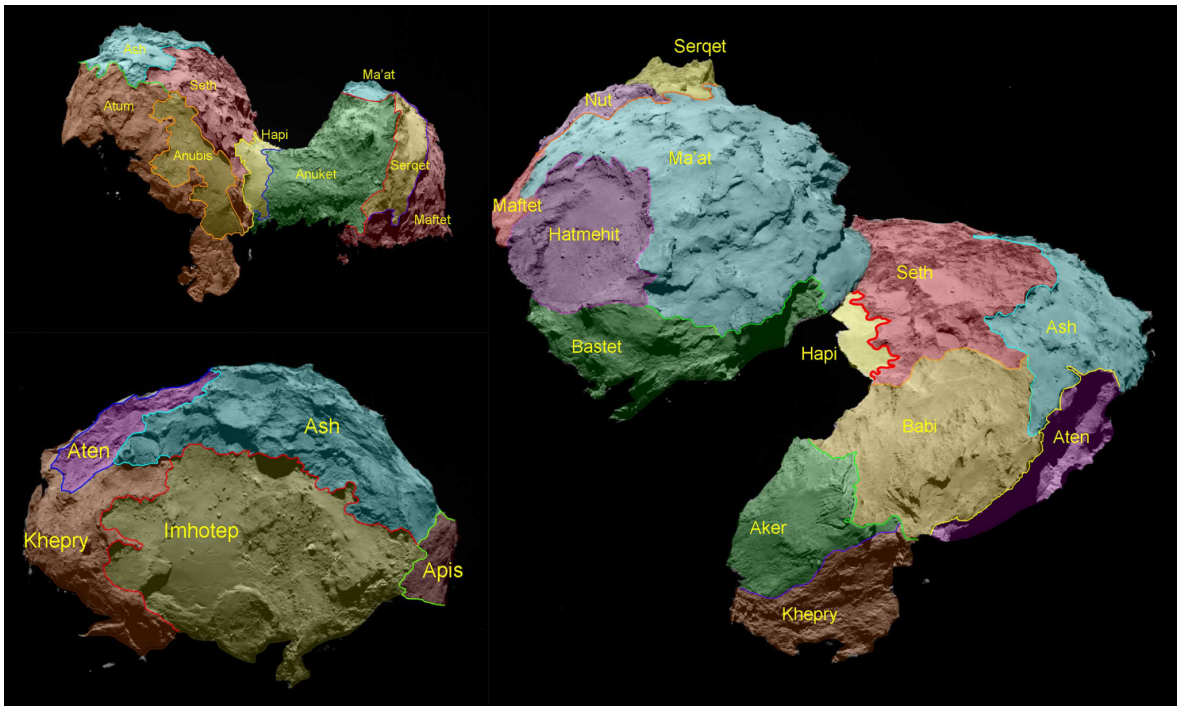

Figure 12: Geological regions of 67P's northern hemisphere (from Thomas *et al.* 2015a).

Thomas *et al.* (2015a) subdivided the geological regions into five categories (Table 1): (1) Exposed consolidated surfaces (also see Section 3.1), (2) large-scale depressions (also see Section 3.2), (3) brittle materials with pits and circular structures (also see Section 3.3), (4) dust-covered terrains, and (5) smooth terrains. Since both (4) and (5) are made of non-consolidated material (NCM), they are described together in Section 3.4.

Within the scope of this study, it is not possible to address the full variety of geological features on the comet's surface, so some limitations were made. One representative example is described for each category in the Sections 3.1 to 3.3. However, the focus

is on NCM airfall deposits (4 & 5) due to its relevance for aeolian-like processes (also see Section 3.4).

Region (Lobe)	**Category**	**Smooth Deposits**	**Dust/Airfall**
Aker (B)	1	X	
Khepry (B)	1	X	
Imhotep (B)	5	X*	
Aten (B)	2		
Ash (B)	4		X*
Seth (B)	3		X
Babi (B)	4		X
Apis (B)	1		
Atum (B)	1		
Anubis (B)	5	X*	
Hapi (N)	5	X*	
Hathor (H)	1		
Anuket (H)	1		X
Ma'at (H)	4		X*
Serqet (H)	1	X	X
Nut (H)	2		
Maftet (H)	1		
Bastet (H)	1		
Hatmehit (H)	2	X	

Table 1: Tabular overview of the northern hemisphere's geological regions on comet 67P/Churyumov-Gerasimenko (abbreviated representation from El-Maarry *et al.* 2015). 'B': body lobe, 'N': neck region, 'H': head lobe. Categories based on Thomas *et al.* 2015a: (1) Exposed consolidated surfaces, (2) large-scale depressions, (3) brittle materials with pits and circular structures, as well as (4) dust-covered terrains, and (5) smooth terrains (both are NCM airfall deposits). 'X' means that the feature occurs, 'X*' indicates that it is the dominant feature of the region.

3.1 Exposed Consolidated Surfaces

Fractured consolidated regions are the most common region type (El-Maarry *et al.* 2015) and represent the comet's exposed surface (El-Maarry *et al.* 2019), for example in the Hathor region (Figure 12). These units appear rocky and robust, although their bulk densities are probably five to ten times lower than those of terrestrial silicates (Thomas *et al.* 2015a). This material contains fractures (Figure 13), cliffs and overhangs, as well as evidence of layering and terracing (Thomas *et al.* 2015a). The fragmentation of exposed consolidated surface (ECS) leads to mass wasting and the presence of boulders (El-Maarry *et al.* 2019, El-Maarry *et al.* 2015).

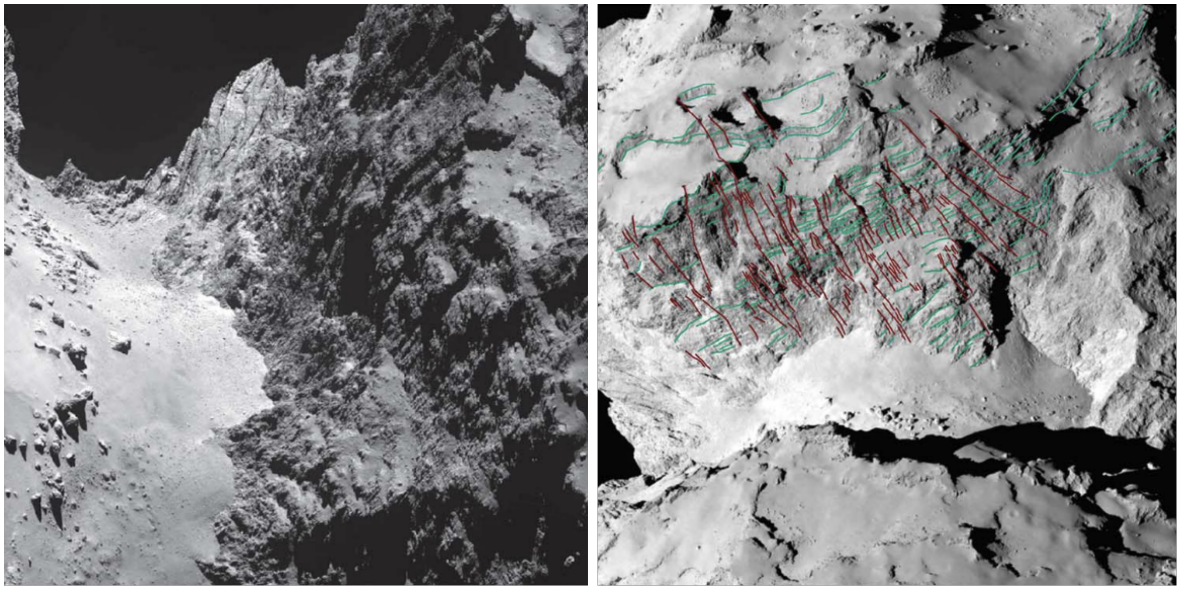

Figure 13: Exposed consolidated surface in the Hathor region, which appears rocky and robust, with horizontal and vertical lineaments (from Thomas *et al.* 2015a).

3.2 Large-scale Depression Structures

The Hatmehit region (Figure 12), located on comet 67P's 'head' lobe, forms a circular depression with a diameter of 900 m and depth of 150 m (Figure 14). Its structure is rather shallow in comparison to bowl-shaped impact craters found on other small bodies (Thomas *et al.* 2015a). A narrow 300 m long linear feature cuts through the region. Fine materials in smoother deposits dominate in this region, and boulders of various sizes lie on the depression's surface (La Forgia *et al.* 2015).

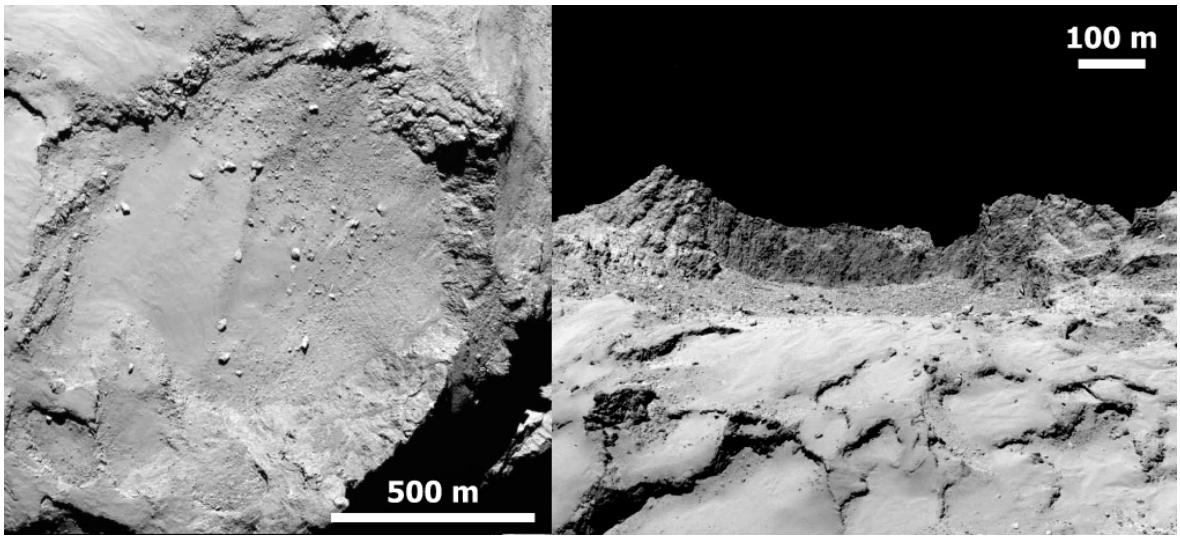

Figure 14: Above and side view of the Hatmehit region (from La Forgia *et al.* 2015).

The origin of the Hatmehit depression is still uncertain. Not only the irregular shape and the depth-to-diameter ratio raise doubts about an impact crater hypothesis. It is also unlikely that the linear feature would have lasted beyond an impact (La Forgia *et al.* 2015).

Pajola *et al.* (2015) proposed an alternative hypothesis, suggesting that the depression could have formed by the process of an underlying volatile-rich layer covered by volatile-poor strata sublimating, and leading to a collapse of the overlying layer forming the structure.

3.3 Brittle Material with Pits & Circular Structures

Brittle material is weakly consolidated, tends to disintegrate while breaking with a high ratio of fine to coarse fragments, and thus produces debris deposits as a result of collapsing (El-Maarry *et al.* 2015). In combination with the low gravity on comet 67P, these collapses show that cometary material has a low tensile strength (Thomas *et al.* 2015a). Brittle material is observed in the Seth region (Figure 15) as well as in the transitions from Ma'at and Ash to other geological regions such as Imhotep (Figure 12). It is also assumed that this brittle material is present everywhere under the NCM airfall deposits in the Ma'at and Ash regions (Thomas *et al.* 2015a, also see Section 3.4).

The Seth region contains a series of flat-floored, steep-walled pits with debris on the surface that in some cases, probably, originates from the collapsed walls (Thomas *et al.* 2015a). The Hapi-facing wall (towards the comet's neck) of those pits is missing in numerous examples due to collapsing (El-Maarry *et al.* 2015). The pits range from 50 to 300 m in diameter and 10 to 200 m in depth (Sierks *et al.* 2015).

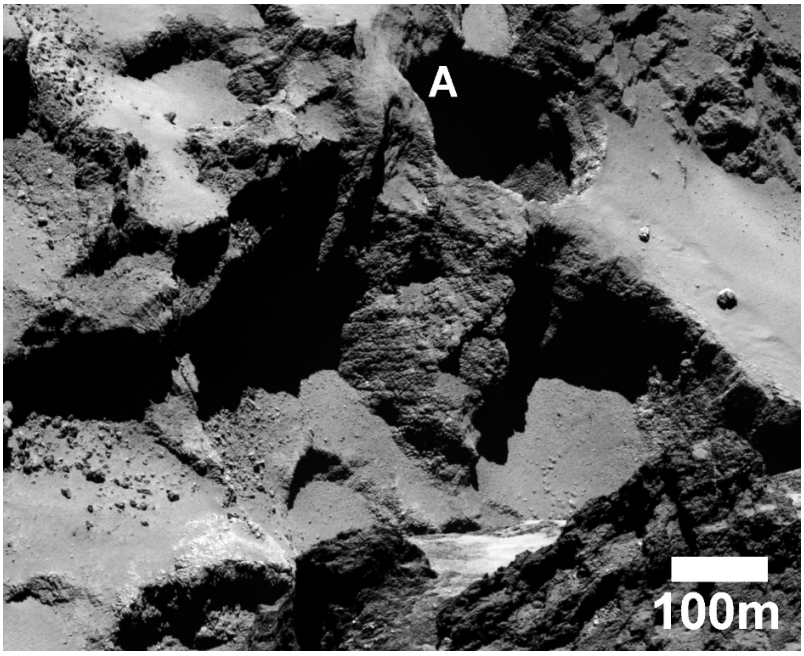

Figure 15: Circular pit (indicated with an A) in the Seth region with brittle material that forms talus- and rockfall-like deposits, visible especially in the image's bottom left quadrant (from El-Maarry *et al.* 2015).

3.4 Non-Consolidated Material with Wind-Tail-like Features

As introduced previously in Section 2.2, in the active phase of a comet approaching the Sun, material gets ejected by jets. This happens, because of sublimation-driven outgassing, which leads to forming a coma around the comet, and develops a transient atmosphere that interacts with the surface by transporting materials (El-Maarry *et al.* 2019). In addition, ejected particles fall back to the comet's surface in NCM airfall deposits (El-Maarry *et al.* 2019). NCM stands for 'non-consolidated material' and covers nearly 20% of the total comet's surface particulary in the northern hemisphere (Figure 16).

This Section will describe, in detail, the presence of NCM airfall deposits on the surface of comet 67P. Since both the dust-covered and smooth terrains (also see Section 3) are made of NCM airfall layers, they are both described together.

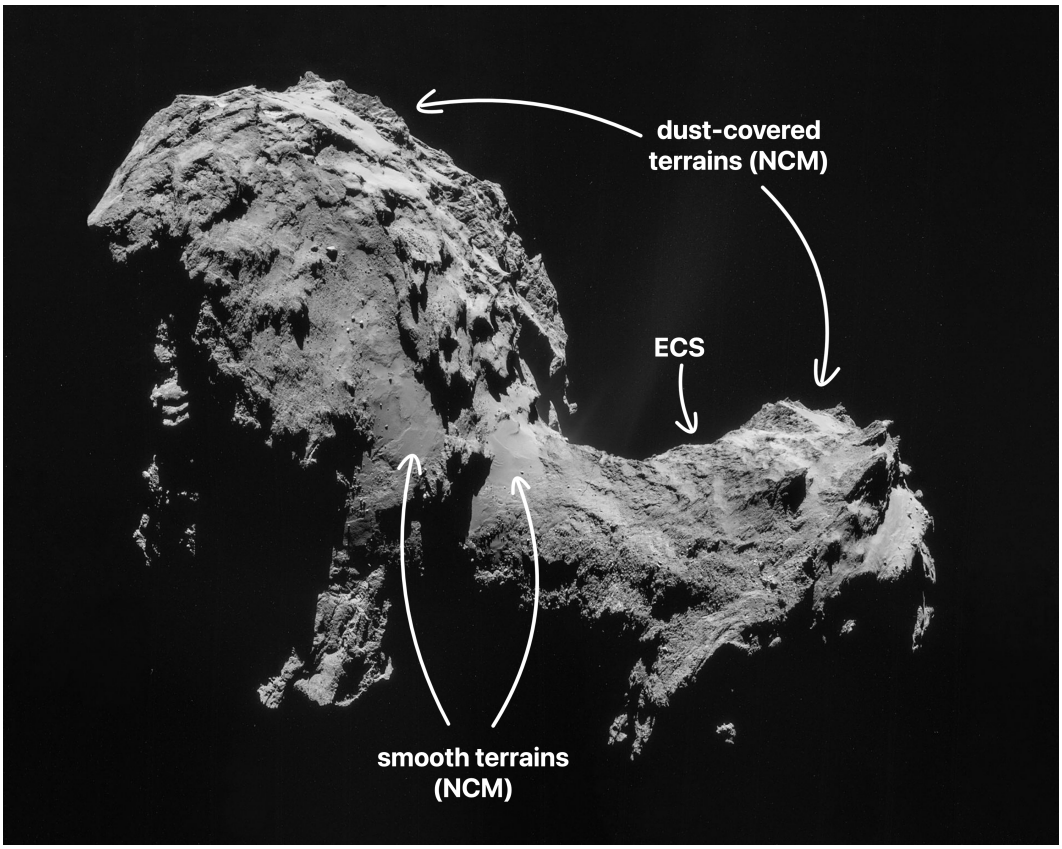

Figure 16: Terrains in the northern hemisphere of comet 67P, NCM stands for 'non-consolidated material', ECS is 'exposed consolidated surface' (El-Maarry *et al.* 2019).

There are two settings where NCM airfall deposits appear on the surface of comet 67P, which are influenced by the topography (Figure 16): (i) In high altitudes (with a high gravitational potential), thin (a few meters) deposits form dust-covered terrains, and (ii) in lower altitudes (with a low gravitational potential), thick deposits of smooth terrains occur (El-Maarry *et al.* 2019).

It is expected that both NCM airfall deposits, dust-covered and smooth terrains, have the same initial composition of grains (Figure 17), with the largest ones a few tens of centimeters in grain size, and spatial inhomogeneities in the size distribution (Auger *et al.* 2015). However, the location and thickness of NCM layers could influence the effects of weathering and erosion. The NCMs probably are the weathering products of consolidated material that were ejected due to cometary activity and subsequently redeposited on the surface (El-Maarry *et al.* 2019).

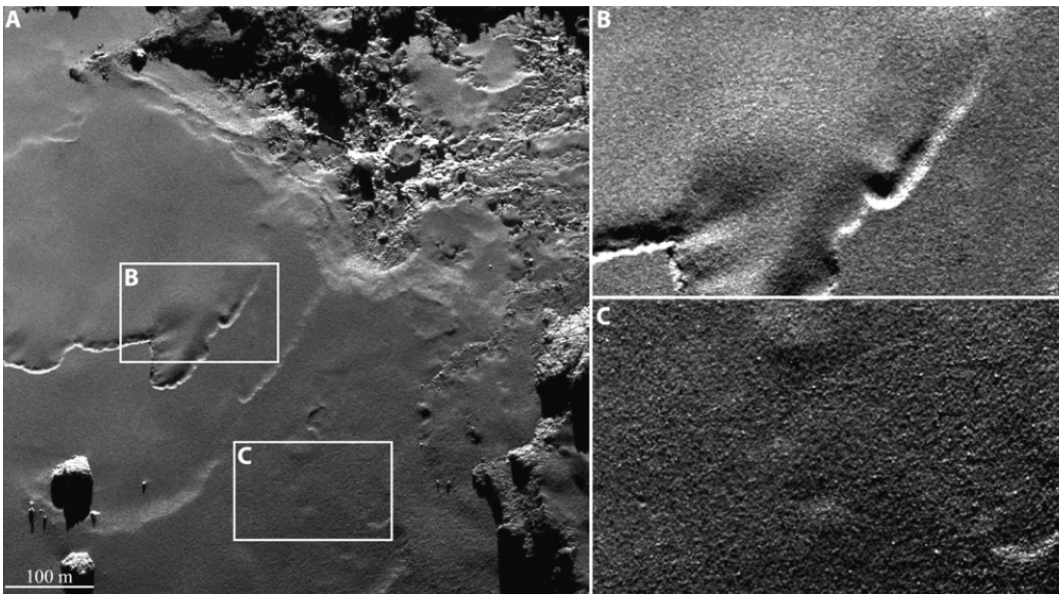

Figure 17: Close-up view of two sites in the Imhotep region, showing fine material that forms the smooth terrains (from Auger *et al.* 2015). At the edges it looks like the NCM airfall deposits are layered (Thomas *et al.* 2015a).

In the southern hemisphere of comet 67P, NCM airfall deposits do not appear due to the absence of wide-scale smooth terrains and dust coatings. This is caused by the higher insolation that the southern hemisphere received during the short but intense summer associated with the perihelion passage (El-Maarry *et al.* 2016).

Dust-covered Terrains

The Ma'at and Ash regions (Figure 12), in particular, are covered by dust (Table 1). It is important to note that the word 'dust' does not imply a specific size range (Thomas *et al.* 2015a). The deposits are fine-grained and mostly homogeneous at the present resolution limit. Large-area outcrops of underlying units still can be observed. Dust-covered terrains are widely distributed, and show signs of mobilisation (El-Maarry *et al.* 2015) such as erosion and remobilisation (El-Maarry *et al.* 2019).

Several dune-like features were detected on comet 67P that are uniformly axis-oriented (La Forgia *et al.* 2015), which may be the result of aeolian-like processes transporting dust over the comet's surface (Thomas *et al.* 2015a). Since there is a preferential orientation, it is suggested that it might be longitudinal dune-like features (Thomas *et al.* 2015b), although the term 'dune' does not imply the same formation processes like of aeolian dunes on planets with atmospheres, but is used here due to the similar morphological appearance. These structures are arranged uniformly along their longest axis and are located in relatively flat areas, where the slope is lower than 10% (La Forgia *et al.* 2015).

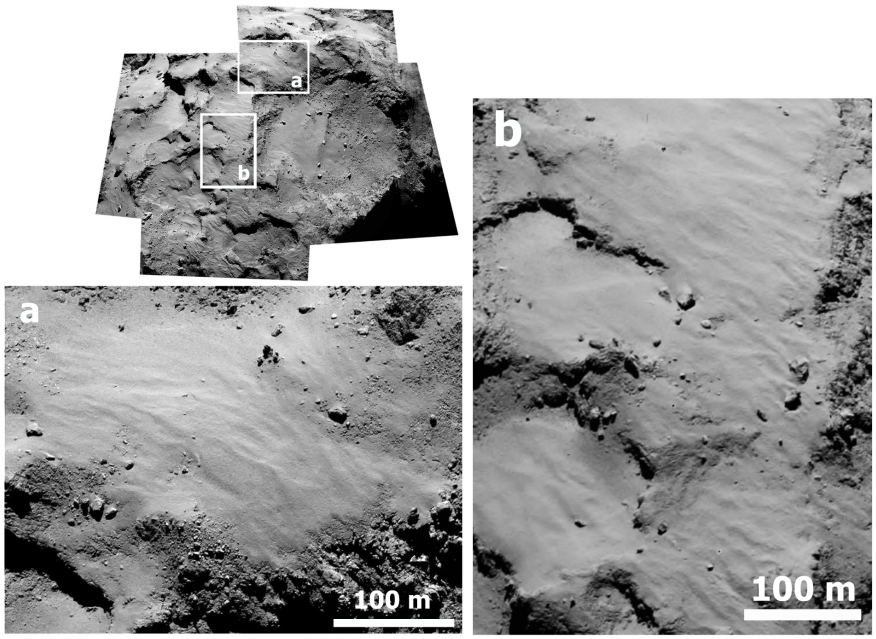

Figure 18: Dune-like structures observed in the Ma'at and Hatmetit regions of comet 67P (from La Forgia *et al.* 2015).

Smooth Terrains

The dominant features of the Imhotep and Hapi regions are smooth deposits (Table 1), where boulders are rare (Thomas *et al.* 2015a). The smooth terrains are made of non-cohesive materials that are thick enough to cover the underlying units and form broadly flat surfaces (El-Maarry *et al.* 2019, El-Maarry *et al.* 2015).

The majority of the smooth deposits in the Imhotep region are contained in the region's gravitational lows, and only in areas where the incline is lower than 15°. The largest area, where smooth terrains have been identified, is located in the centre of the region, and is with less than 5° particularly flat (Figure 19). The thickness of the smooth deposits decreases upslope towards the region's edges (Auger *et al.* 2015).

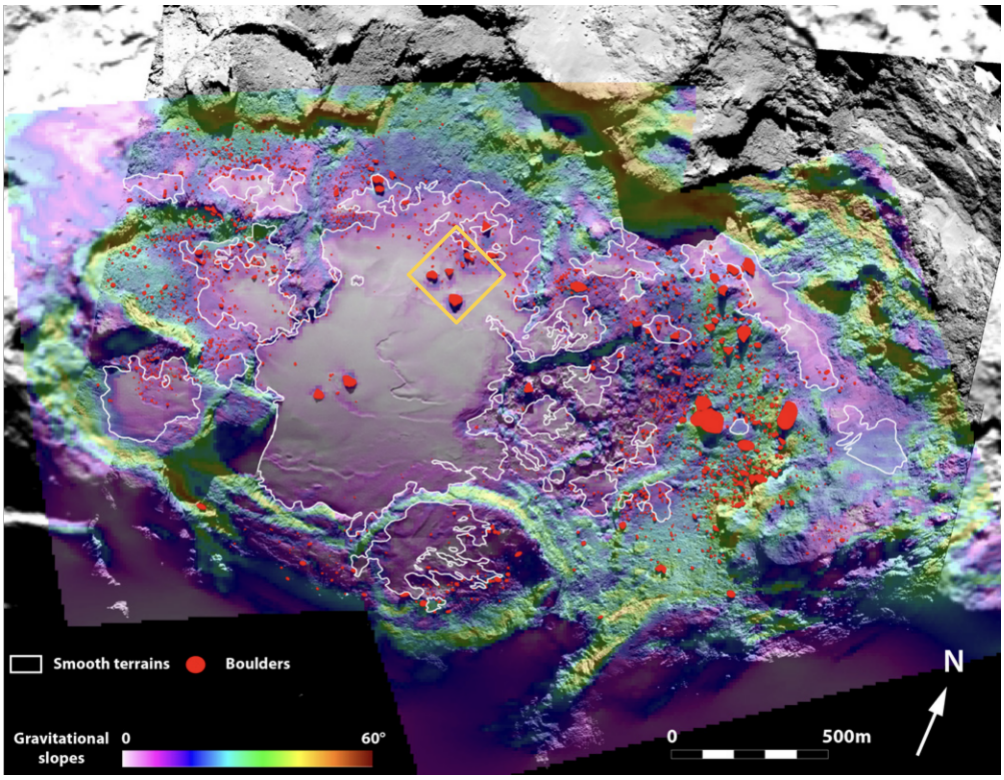

Figure 19: Gravitational inclines in the Imhotep region with the borders of smooth deposits, and boulders shown in red (from Auger *et al.* 2015). The yellow square shows the image area shown in Figure 43.

One distinctive feature observed in the Hapi region is a ripple field (Figure 20), which suggests that aeolian-like processes may be of significance (El-Maarry *et al.* 2015). This

observation implies that the Hapi region is fundamentally different from the Imhotep region (Thomas *et al.* 2015a).

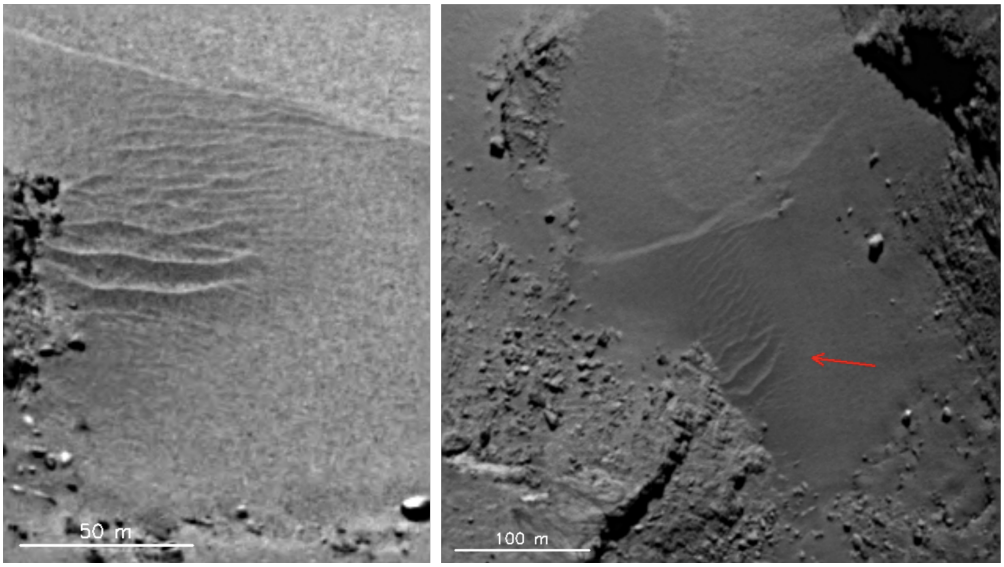

Figure 20: (Left): Aeolian-like ripple field in the Hapi region. (Right): Lateral view of the ripples (red arrow) (from Thomas *et al.* 2015b).

It is proposed by Thomas *et al.* (2015b) to explain the ripple-like bedforms, observed in 67P's Hapi region, by the depositional airfall-driven process originating from above, with slower speed particles moving along the surface, possibly driven by gas drag and/or the gravitational slope (Figure 21).

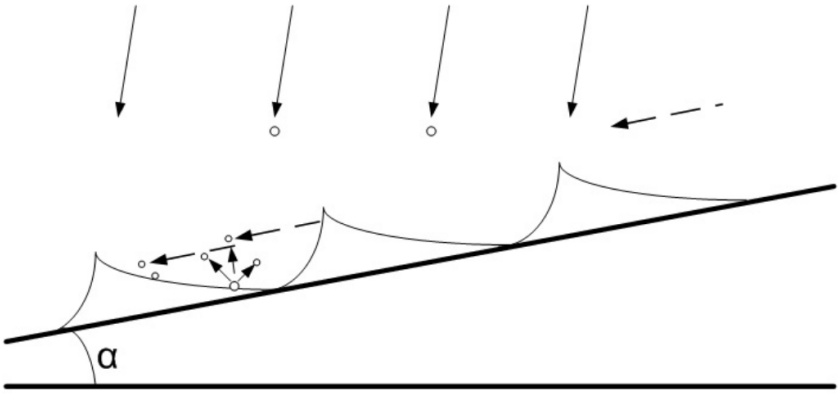

Figure 21: Scheme of the proposed airfall-driven depositional process, producing the ripple-like structures in the Hapi region, and the widely distributed NCM layer on the surface of comet 67P (after Thomas *et al.* 2015b).

Wind-Tail-like Features

Wind-tail-like features on comet 67P appear in association with boulders acting as obstacles, behind which material accumulates in the form of an elongated wedge (Figure 22). The similarity to aeolian wind tails on Earth is astonishing (Figure 2).

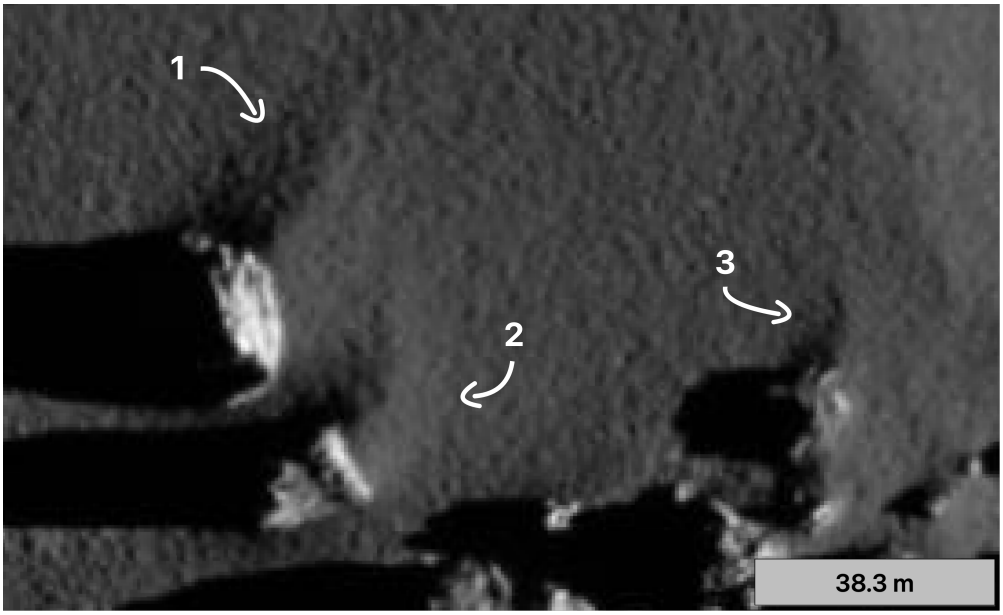

Figure 22: Example of three wind-tail-like features in 67P's Hapi region.

Based on the results of previous studies, all wind-tail-like features found on the surface of comet 67P occur in areas covered with airfall-like NCM deposits (Sachse *et al.* 2022). It is important to note that the term 'wind-tail-like feature' is not to imply that wind is involved in the deposition of the structures, but is used because of the morphological similarity to wind tails as aeolian features commonly observed on planets with atmospheres such as Earth and Mars (also see Section 1.1). These feature's deposition on comet 67P is suggested being of erosional nature as a result of the abrasion of the sand bed induced by airfall particles (Thomas *et al.* 2015a).

In contrast to the aeolian (by saltation) and subaqueous (by traction, saltation and suspension) transport mechanisms (Jia *et al.* 2017, Nichols 2009), particles in a cometary environment are moved by (i) traction, and (ii) rebounding to the surface in an airfall process (Jia *et al.* 2017) after being ejected to the comet's coma due to sublimation-driven outgassing (Figure 23).

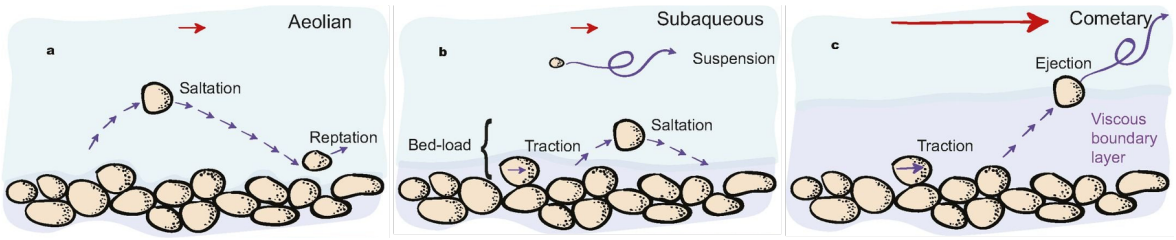

Figure 23: Material transport mechanisms in (a) aeolian, (b) subaqueous, and (c) cometary environments (from Jia *et al.* 2017).

As described previously (also see Section 2.2), cometary activity has a depositional aspect, forming the widely distributed NCM airfall deposits on the surface of comet 67P. Non-escaping dust particles are transported and resediment by an airfall process to the surface (Thomas *et al.* 2015b).

The formation of wind-tail-like features on the surface of comet 67P is assumed to be an erosive process, which Mottola *et al.* (2015) proposed based on simulations that resulted in a model forming wind-tail-like features due to abrasion of the surface by impinging particles (by airfall processes) except for areas that are shielded by obstacles, and therefore are protected by for example boulders, behind which the wind-tail-like features appear (Figure 24).

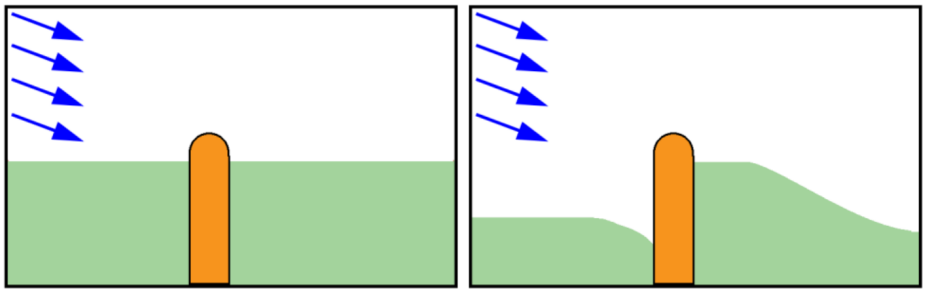

Figure 24: Simulation results reproducing the basic morphology of the observed wind-tail-like features on comet 67P, suggesting the erosional rather than depositional nature (after Mottola *et al.* 2015).

4 Material and Methods

The goal of this study was to identify and measure the extent of wind-tail-like features as well as the boulders they are associated with, on the surface of comet 67P. Previous studies have conducted this work for the pre-perihelion period (Sachse *et al.* 2022), however, as 67P showed significant surface changes after its perihelion passage (El-Maarry *et al.* 2017), I wanted to examine the variation of wind-tail-like features after the comets high activity phase. This was carried out using remote sensing images of ESA's Rosetta mission.

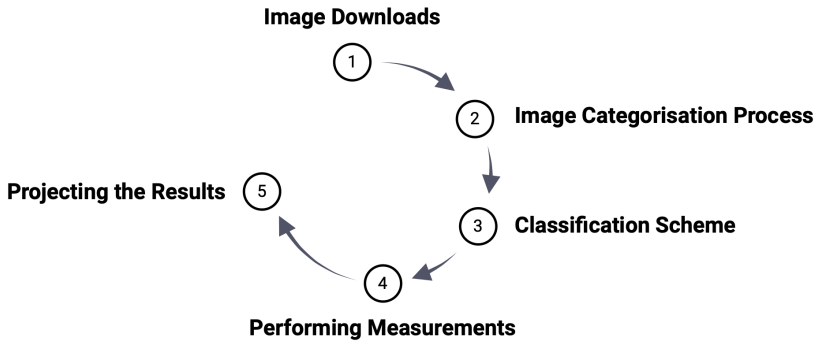

Figure 25: Main tasks in conducting the analysis of this BSc thesis.

This section outlines the main tasks that were performed to conduct the analysis (Figure 25). The parameters in ESA's Planetary Science Archive (hereafter PSA), which were set to download the images (Section 4.1), will be introduced. Subsequently, the image categorisation process will be described: The images were manually reviewed frame-by-frame and categorised according to the presence of wind-tail-like features (Section 4.2). For this, the wind-tail-like features have been categorised into two different types A and B because they show different morphological attributes. Geometric measurements of the wind-tail-like features were carried out using the Small Body Mapping Tool (SBMT) software (Ernst *et al.* 2018). A number of different parameters were identified and measured, namely, (i) length of the wind-tail-like feature, (ii) boulder dimensions, and, (iii) coordinates of the boulder top (Section 4.3). These were then illustrated using the Paraview software with the results being presented in a 3D overview map which shows the distribution and orientation of the wind-tail-like structures on the surface of comet 67P (Section 4.4).

4.1 Data

The remote sensing images from ESA's Rosetta mission of the surface of comet 67P were downloaded from ESA's PSA. Images are abundant (c. 100,000) exceeding the ability to analyse them individually. Thus, search parameters were introduced. The filter settings for narrowing the search are shown in Table 2, the reasons why these were applied are described below.

Parameters	**Filter Settings**
Mission	Rosetta Orbiter
Instrument	OSIRIS Narrow Angle Camera (NAC)
Observation Period	01 May to 31 July 2016
Processing Level	4
Filter	22

Table 2: Parameters set as filter settings for narrowing the search in ESA's PSA.

Instrument: OSIRIS Narrow Angle Camera (NAC)

The OSIRIS module of the Rosetta spacecraft consists of two cameras, a high-resolution telephoto camera (NAC) and a wide-angle camera (WAC). The purpose of NAC was to generate detailed images of the comet's surface from distances of more than 500,000 km to 1 km. In contrast, the WAC was designed to obtain images of the comet's nucleus environment in order to study the various weak gas and dust features (Deller & Sierks 2022, Tubiana *et al.* 2015). In order to identify small scale wind-tail-like features, high resolution images were needed and, therefore, NAC images were analysed for the purposes of this BSc thesis.

Observation Period: 1 May to 31 July 2016

The perihelion transit of comet 67P, its closest distance to the sun, occurred on 13 August 2015 (Barrington *et al.* 2023). A reasonable study period after 13 August 2015 had to be identified because the data would be compared with pre-perihelion findings of previous studies (e.g. Sachse *et al.* 2022). The observation time from 1 May to 31 July 2016 (Figure 26) was chosen because during these dates the distance between the spacecraft and the comet was minimal (Taylor *et al.* 2017).

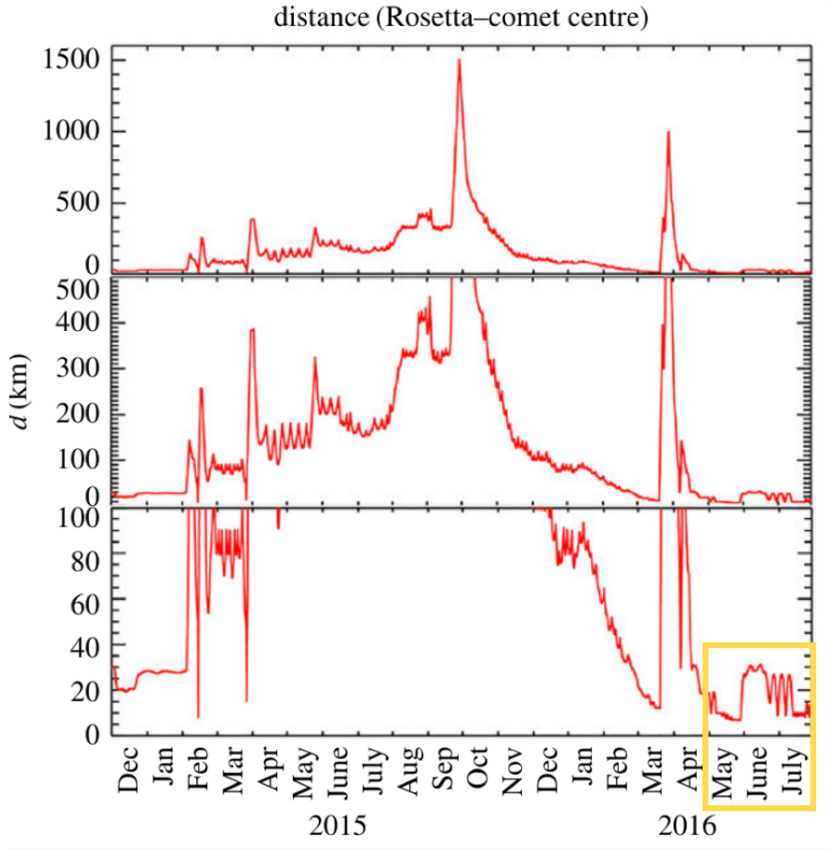

Figure 26: Changes in distance between the Rosetta Orbiter and the centre of comet 67P in the period from December 2014 to July 2016 (from Taylor *et al.* 2017), the perihelion took place on 13 August 2015 (Barrington *et al.* 2023), the observation period used for this BSc thesis is highlighted with a yellow square.

Processing Level: 4

For processing level 4 images, the data is calibrated and resampled (Deller & Sierks 2022, Tubiana *et al.* 2015), which increases the overall data quality with improving processing level. In the observation period, there are 1858 images available in ESA's PSA for processing level 4 and 78 images less for level 5 (1780 images). The image quality was compared using a random sample check, since the images are essentially identical, but with a higher degree of information derivation (e.g. through pixel corrections). As no relevant differences in image quality could be identified between level 4 and 5 data (which are the two highest levels available). It was, therefore, decided to use the level 4 images, since the amount of images available for use as a database for this study is slightly greater.

Filter: 22

The NAC has a set of 11 broad-band filters with four focusing plates. The spectral properties are determined by the filters. The focussing plates control the focus of the camera and are used for objects that are further than 2500 m away from the camera (Deller & Sierks 2022, Tubiana *et al.* 2015). Filter 22 was selected to reduce the amount of data. This is because the filters were often changed in quick succession so that almost identical images were captured (just in another spectrum). As only one colour was required, images with filter 22 were used as a default for this BSc thesis. This means that the far focus plates (FFP) were applied in combination with the orange filter in the visible light spectrum (Deller & Sierks 2022, Tubiana *et al.* 2015).

4.2 Image Categorisation Process & Classification Scheme

During the image categorisation process, 1858 images previously downloaded from ESA's PSA were manually reviewed frame-by-frame and categorised according to the presence of wind-tail-like features. The aim was to identify the images on which wind-tail-like features appear in order to measure them in the next step with the Small Body Mapping Tool (SBMT) software (Ernst *et al.* 2018). The image categorisation process was carried out over several steps (Figure 27), which will be detailed below:

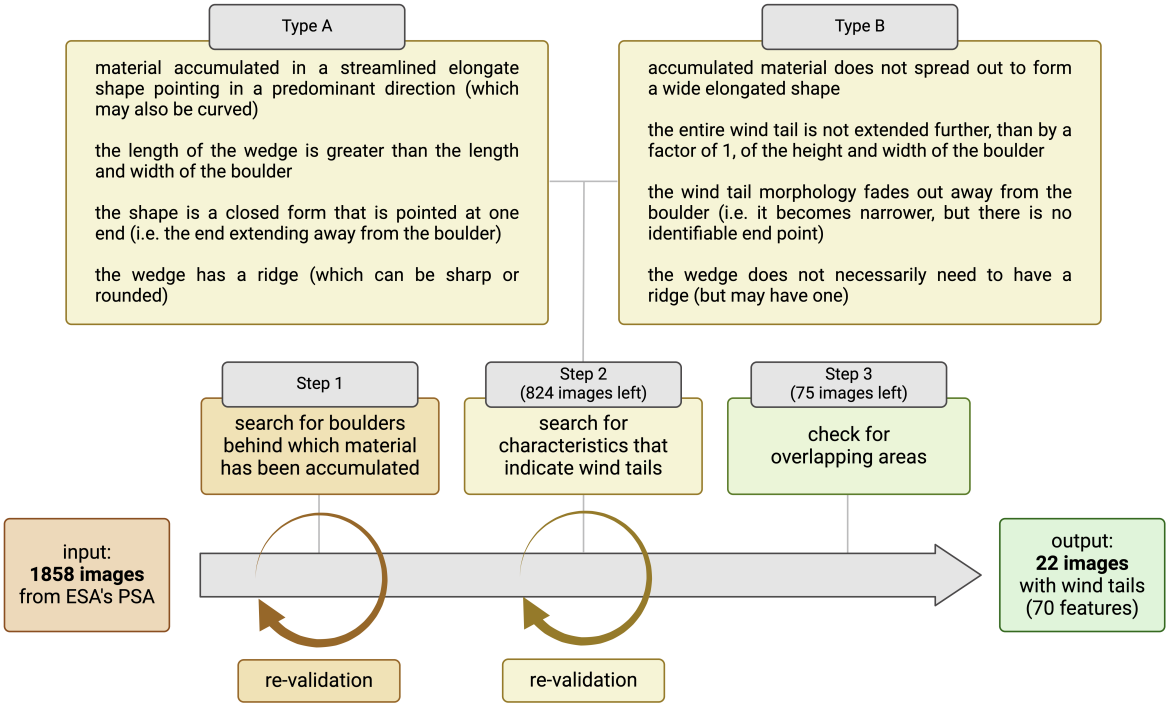

Figure 27: Flowchart of the image categorisation process.

Step 1

All images were viewed in a complete scan of the database. Images with no boulders behind which a wind-tail-like feature might be expected, were removed. At first, this means that boulders were searched behind which it appears like material has accumulated (Figure 27). Subsequently, all of the images were rechecked in order to validate the original decision. At this stage of the analysis, 824 images remained.

Step 2

The remaining images were then individually analysed, in detail, in an up close view to identify whether there was a characteristic found that indicates a wind-tail-like feature (Figure 27). For this purpose, a scheme for classifying wind-tail-like features was determined, based on their different morphological attributes (which are described in Figure 27). The recognised wind-tail-like features were categorised into type A (Figure 28) and type B (Figure 29). Once again, the images sorted out in this step were reexamined to validate the sorting. After this, a total of 75 images were flagged for the next phase.

Step 3

The remaining 75 images were finally evaluated to determine whether their perspective areas overlap. Such features may occur, as a result of the fact that the spacecraft orbits the comet several times and images are therefore taken from different perspectives. In the end, 22 images with wind-tail-like features were identified.

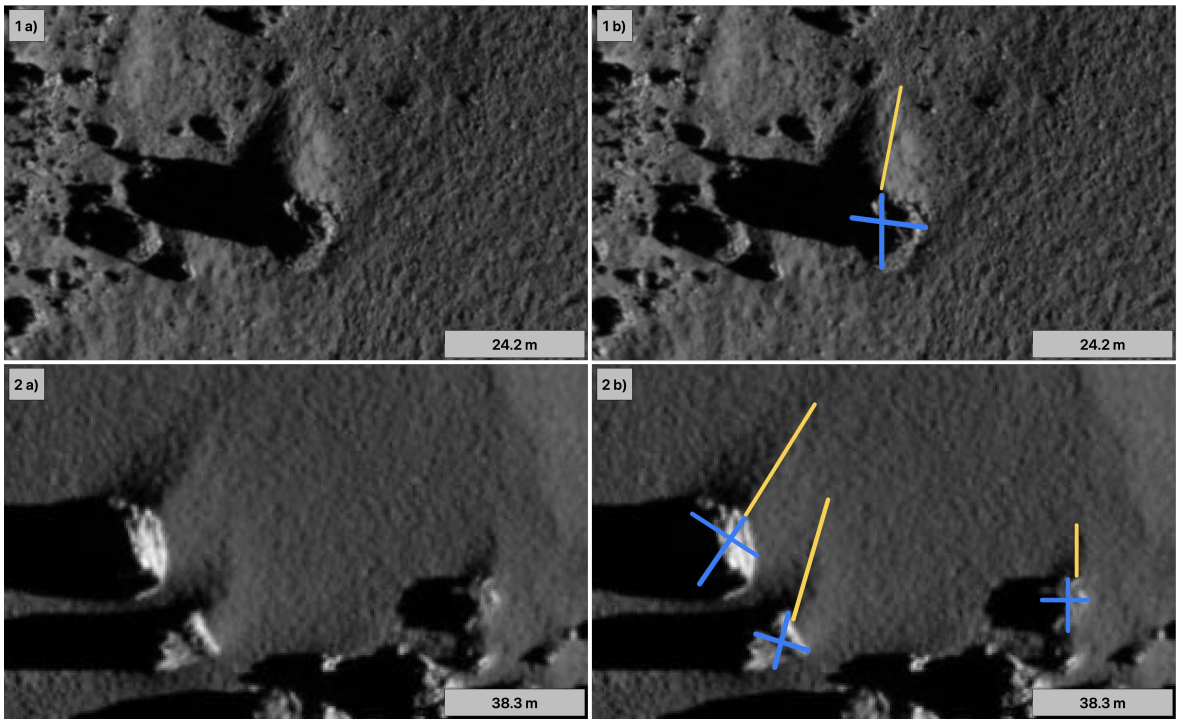

Figure 28: Examples for wind-tail-like features 'type A'. 1a/2a: Original image, 2a/2b: Same image but with yellow lines indicating the length of the wind-tail-like features and blue lines showing the length and width of the boulder. 'Type A' characteristics are (i) material accumulated in a streamlined elongate shape pointing in a predominant direction (which may also be curved), (ii) the length of the wedge is greater than the length and width of the boulder, (iii) the shape is a closed form that is pointed at one end (i.e. the end extending away from the boulder), and (iv) the wedge has a ridge (which can be sharp or rounded).

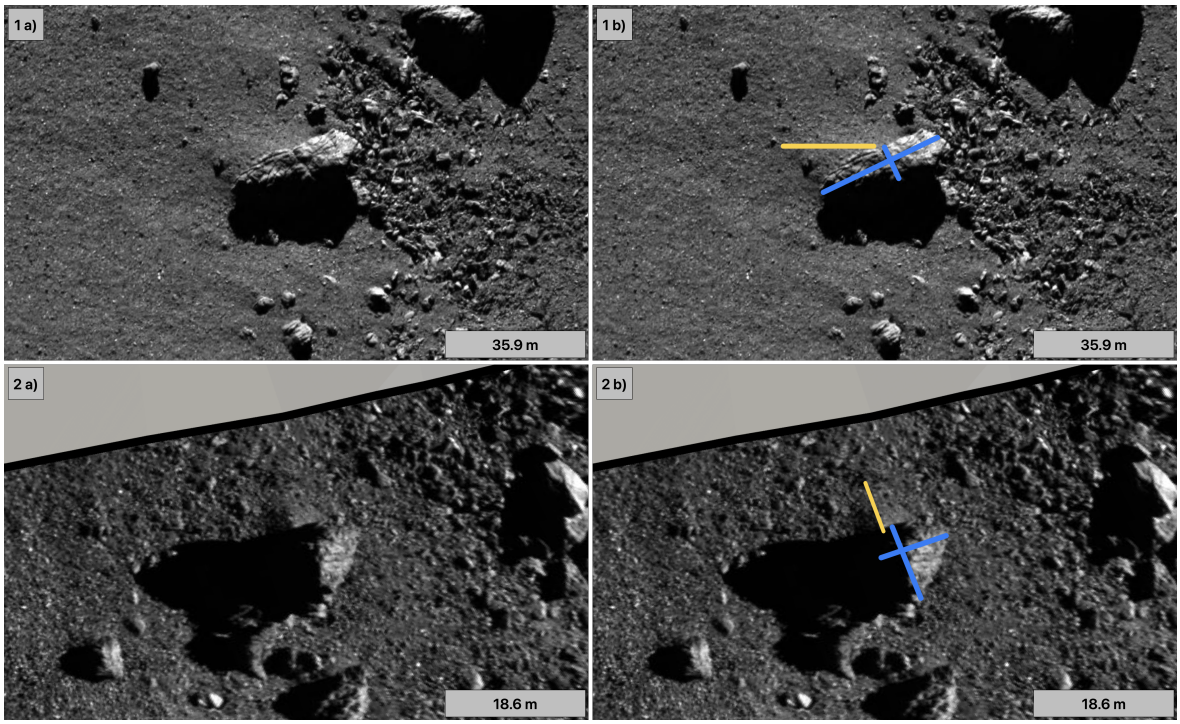

Figure 29: Examples for wind-tail-like features 'type B'. 1a/2a: Original image, 2a/2b: Same image but with yellow lines indicating the length of the wind-tail-like features and blue lines showing the length and width of the boulder. 'Type B' characteristics are (i) accumulated material does not spread out to form a wide elongated shape, (ii) the entire wind tail is not extended further, than by a factor of 1, of the height and width of the boulder, (iii) the wind tail morphology fades out away from the boulder (i.e. it becomes narrower, but there is no identifiable end point), and (iv) the wedge does not necessarily need to have a ridge (but may have one).

4.3 Performing Measurements with the SBMT

In order to perform geometric measurements on the highly irregularly shaped comet, the remote sensing images had to be projected onto the three-dimensional shape model of comet 67P. The Small Body Mapping Tool (SBMT) from the Applied Physics Laboratory at John Hopkins University (Ernst *et al.* 2018) was used to achieve this (Figure 30).

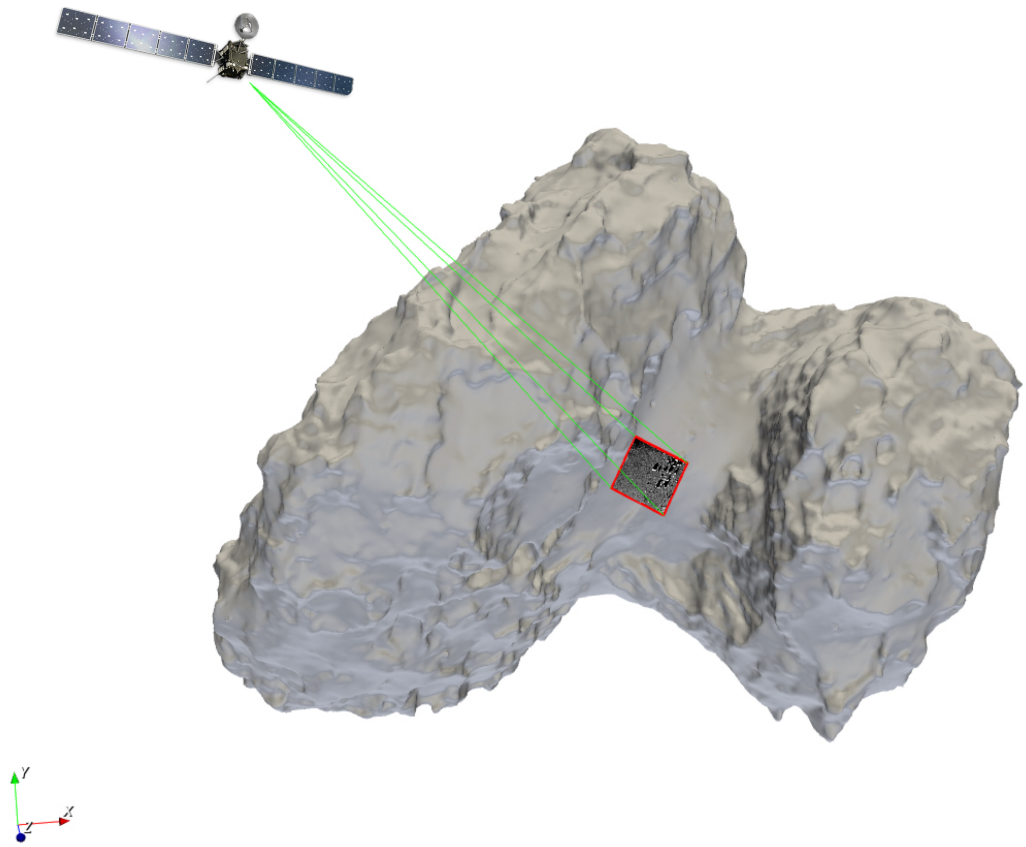

Figure 30: Example of a projected image on shape model 'DLR SHAP4S' by Preusker *et al.* 2015 in the neck-region of comet 67P/Churyumov-Gerasimenko, produced with the SBMT. The position of the orbiter at the moment the image was captured is highlighted by green lines. The edges of the image are marked in red. The space probe is not accurate neighter in scale nor in orientation.

The purpose of the SBMT is to enable large amounts of data generated by space missions to be accessed, visualised, and analysed as easily as possible. In addition, mapping small bodies (e.g. asteroids and comets) is problematic since the two-dimensional map projections strongly distort features on their irregularly-shaped bodies. The SMBT ad-

dresses these challenges by enabling researchers to locate and project images onto shape models and to map, mark, and label the various surface features on the irregularly-shaped bodies (Ernst *et al.* 2018).

Metadata for each image downloaded was archived from ESA's Planetary Science Archive (PSA), but it turned out that PSA's .LBL files, which are text-files that contain detailed information about the individual image (e.g. orbital coordinates of the Rosetta spacecraft when taking the image, and many more parameters), could not be read by the SMBT and would have needed significant resources to be utilized for the projection. In fact, this would have required mathematically calculating the pointing files required for the projection in the SBMT myself. This procedure, given its complexity as well as the time investment required, almost jeopardised the progress of this BSc project since it clearly exceeded the scope (in terms of time and subject) of the project. As a consequence, the SBMT development team of the Applied Physics Laboratory at John Hopkins University was contacted and thankfully the .SUM pointing files, that are required by the SMBT, were supplied by the scientists there.

The various parameters that were measured with the SBMT are listed below (Figure 3):

1. **Length of the wind-tail-like feature**:
   The distance between the tip of a wind-tail-like feature, where the morphological appearance blends into the underlying texture, and the contact point of the deposit with the boulder (Figure 32).

2. **Boulder dimensions**:
   The length and width between the borders of the boulder, that visually stand out from the surface below. The angle between the measured lines is perpendicular (Figure 32).

3. **Coordinates of the boulder top**:
   Boulders are not resolved on the shape model, because the resolution of the 2D remote sensing images (2.31 m/pixel on average of the images analysed in this BSc thesis) is much higher than the resolution of the 3D shape model (158.41 m^2/facet). Thus, the wind-tail-like features are projected as flat features

onto the surface, which does not represent reality. To estimate the height of the boulder and wind-tail-like feature, I measured a boulder's width and length and averaged the value. I further assumed that the boulder was half buried in the comets regolith and thus used half of this value as the boulder's / wind-tail-like feature's height (Figure 31). I note that this is a very rough estimate, however it is consistent with the work of Sachse *et al.* (2022) and Otto *et al.* (2017).

In order to calculate the orientation of the wind-tail-like features as a vector in the 3D spatial environment, the surface normal of the facet on which the boulder and the wind-tail-like feature are located was determined. For this, three points of the relevant facets were measured (Figure 32), from which the surface normal then was calculated by utilising the cross product (see project report for details).

In the next step, the estimated height of the boulder was added using the normal vector, which is orthogonal to the facet of the shape model on which the boulder was located (Figure 31). This results in the 3D coordinates of the top of the boulder. Based on this information, the inclined vector pointing from the boulder top to the wind-tail-like feature tip at the surface could be calculated. This information was required in order to generate a 3D overview map with the correct orientation of the wind-tail-like structures on the surface of comet 67P.

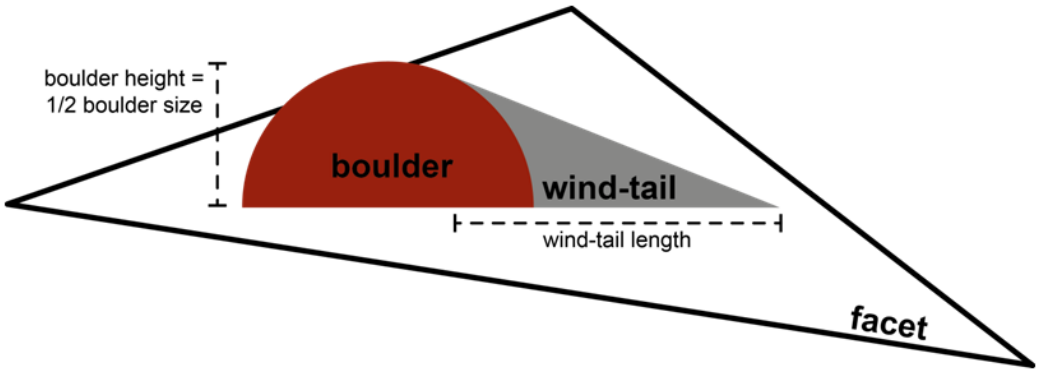

Figure 31: Illustration of the facet on which the wind-tail-like feature and boulder are located. The height of the boulder was estimated as half the mean value of the boulder's width and length, here labeled boulder size (from Otto *et al.* 2017).

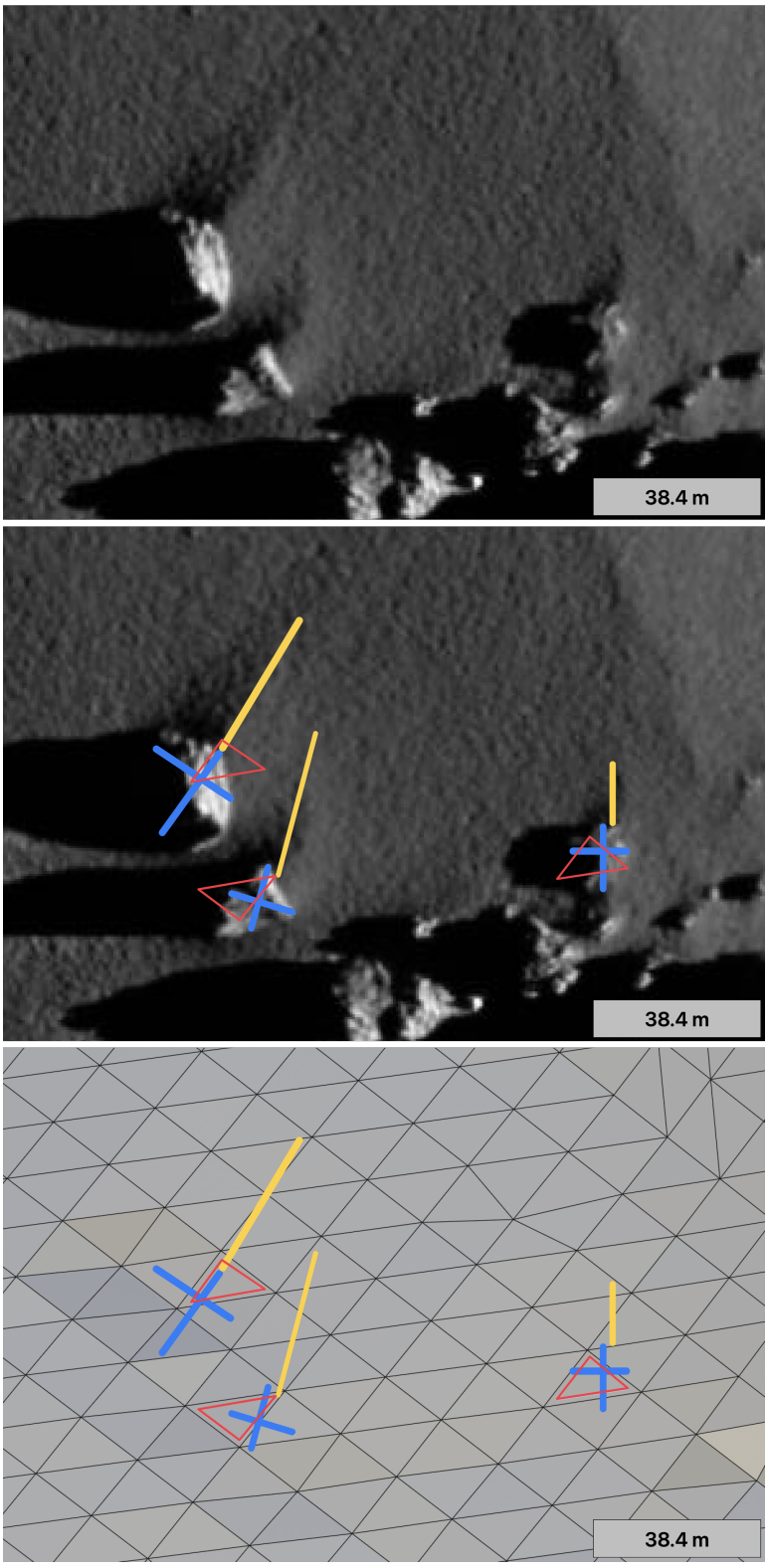

Figure 32: Example image section showing the measured parameters in SBMT (yellow: length of the wind-tail-like feature, blue: boulder dimensions, red: the shape model's plate). Bottom: Equivalent image section with the texture of the shape model, so that the plate on which the boulder is located could be measured.

4.4 Projecting the Results in Paraview

Although the SMBT is a valuable tool to measure and map features it is not well suited to illustrate parameters assigned to mapped features. Therefore the measurements were exported to be used in Paraview. Paraview is an open source software for data analysis and visualisation, written to be used for scientific data sets (Röber 2014). In this BSc thesis, Paraview was, therefore, used to map the measured wind-tail-like features as vectors onto the shape model of comet 67P in order to obtain a 3D overview map of the distribution and orientation of the wind-tail-like structures on the surface.

The shape model used, 'DLR SHAP4S' (Preusker *et al.* 2015) was exported from the SBMT and loaded into Paraview. The geological regions on 67P were obtained from ESA's PSA FTP server (ESA 2024). 'DLR SHAP4S' is actually a pre-perihelion shape model, but the pre- to post-perihelion variation in the shape model should not affect the outcome of this work.

The coordinates exported from the SMBT were provided in Spherical coordinates (latitude [rad], longitude [rad] and radius [km]). As Paraview requires Cartesian coordinates, these values had to be converted. After converting the units from radians [rad] to degrees [°], the Spherical coordinates were transferred into Cartesian coordinates (x [km], y [km], z [km]). All of the calculations necessary made to project the wind-tail-like structures as vectors onto the shape model were performed in Microsoft's EXCEL software and are explained step by step in more detail in the corresponding project report of this BSc thesis.

5 Results

In the observation period from 01 May to 31 July 2016, 1858 images were examined, of which 22 show wind-tail-like structures located behind boulders. The entire comet's illuminated surface was examined, showing that the structures predominantly occur in areas with airfall-like NCM deposits. The images used for measurements in the SBMT were taken from an altitude of 12.3 km with a resolution of 23.1 cm/pixel (both mean values, also see Table 4) by the Rosetta Orbiter. A total of 70 wind-tail-like features were found, of which 27 were classified as type A and 43 as type B (Figures 33 to 35). The average boulder size (mean of the boulder's length and width) is 10.2 m ± 6.7 m (one standard deviation) with a minimum of 2.4 m and a maximum of 36.9 m. The wind-tail-like feature's length is 10.6 m ± 11.0 m with a minimum of 2.0 m and a maximum of 45.0 m. Most features are less than 20 m in length, while the majority of boulders associated with them are less than 16 m in size. The boulder sizes correlate with the length of the wind-tail-like features by a slope fit of 1.04 (Figure 36).

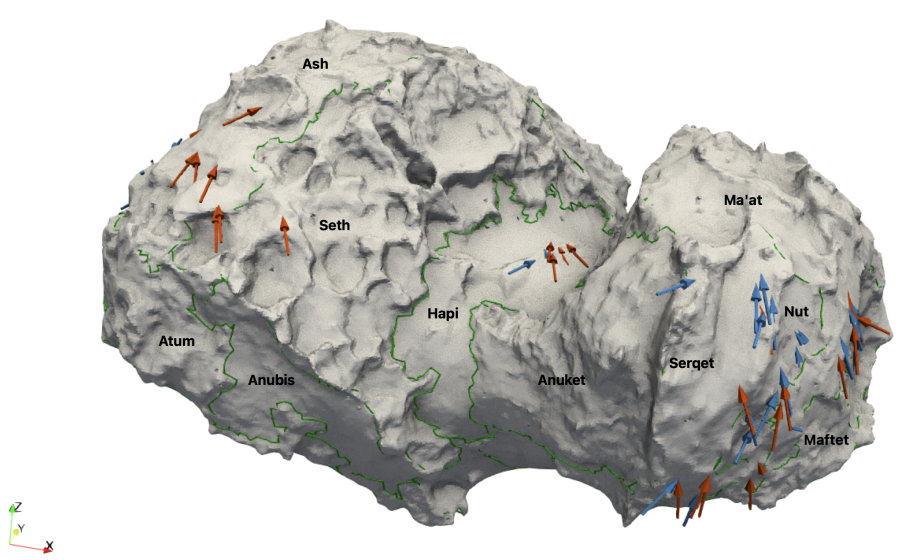

Figure 33: Post-perihelion findings of wind-tail-like features on comet 67P, categorised in 27 type A (orange) and 43 type B (blue) ('front' view). All findings on the 'back', as shown in Figure 35, were categorised as type B. Green lines indicate the boundaries of geological regions.

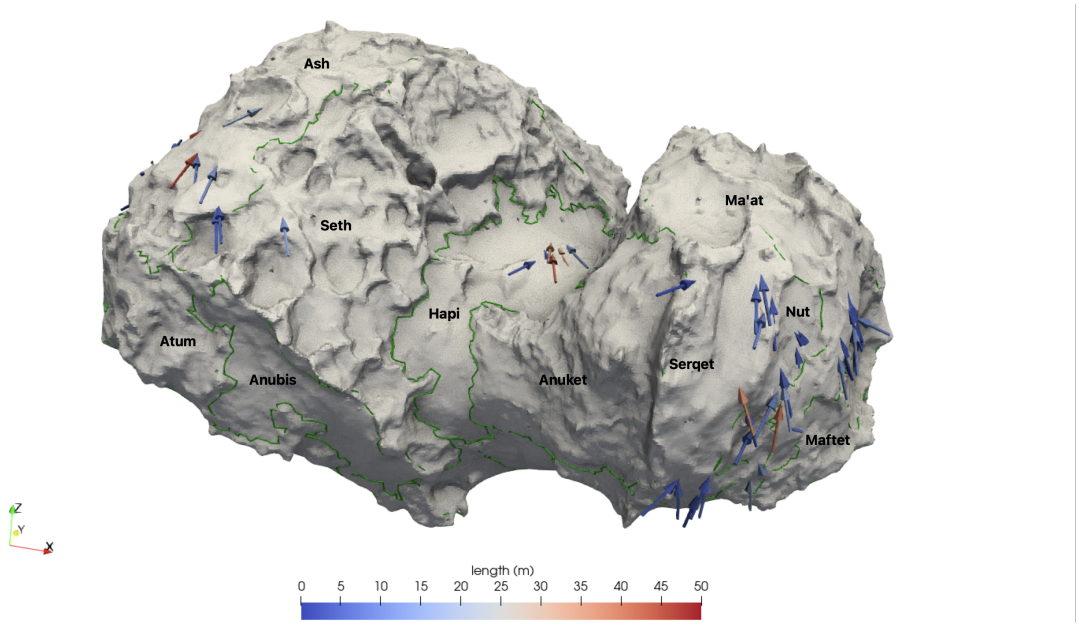

Figure 34: Post-perihelion 3D overview map of the distribution and orientation of wind-tail-like features on the surface of the northern hemisphere of comet 67P ('front' view). The arrows are coloured according to their length. Green lines indicate the boundaries of geological regions.

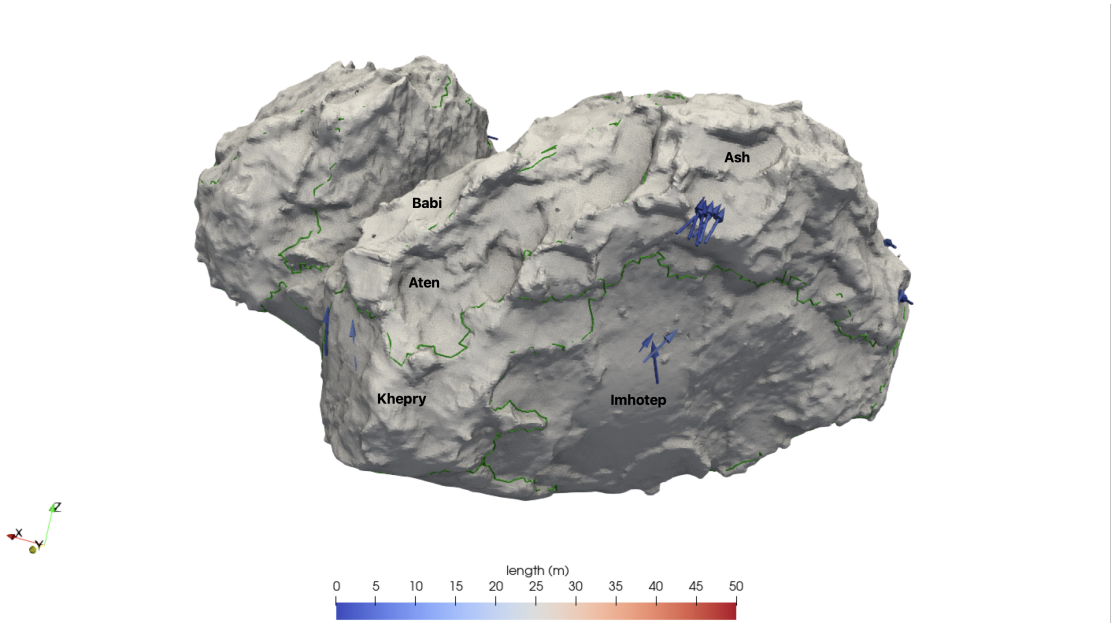

Figure 35: Post-perihelion 3D overview map of the distribution and orientation of wind-tail-like features on the surface of the northern hemisphere of comet 67P ('back' view of the 'body' lobe). The arrows are coloured according to their length. Green lines indicate the boundaries of geological regions.

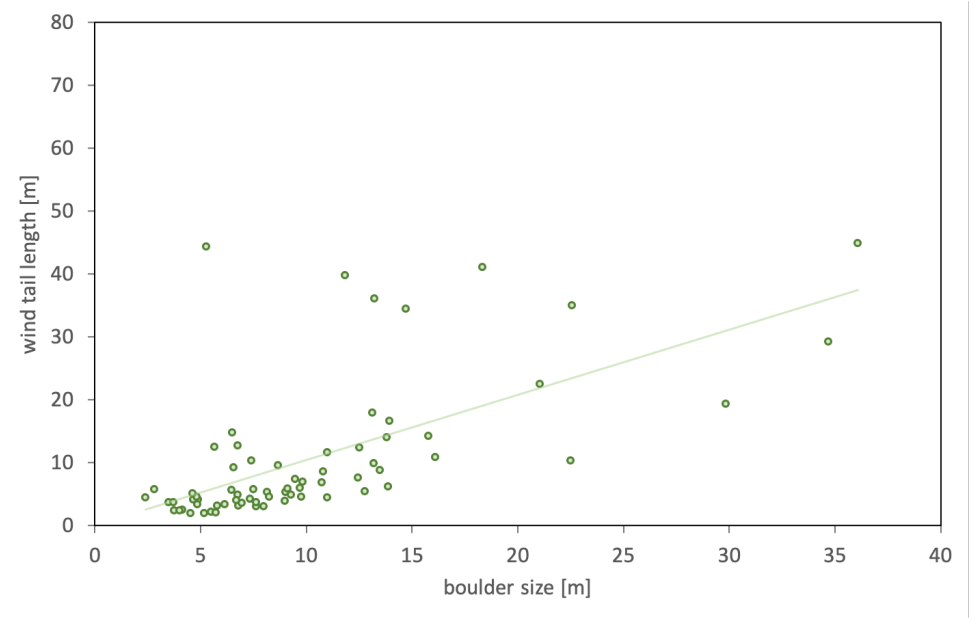

Figure 36: Plot of the boulder sizes (mean of the boulder's length and width) and the lengths of the wind-tail-like features, in the observation period from 01 May to 31 July 2016 (post-perihelion) with 70 features identified (linear slope fit of 1.04).

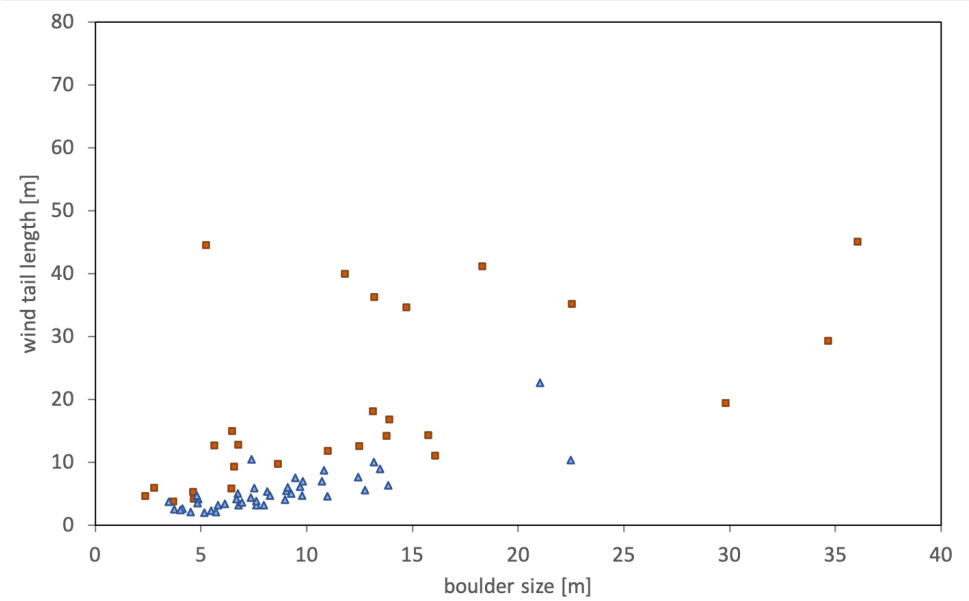

Figure 37: Plot of the boulder sizes (mean of the boulder's length and width) and the lengths of the wind-tail-like features, in the observation period from 01 May to 31 July 2016 (post-perihelion), categorised in 27 type A (orange) and 43 type B (blue).

Cataloged in this BSc thesis, the post-perihelion results show a high concentration of small wind-tail-like features (boulder size $\leq$ 15 m and wind tail length $\leq$ 20 m) (Figure 36).

There are more wind-tail-like features type B (43) than type A (27) on the surface of comet 67P (Figure 37). To remind, the 'type A' characteristics are (i) material accumulated in a streamlined elongate shape pointing in a predominant direction (which may also be curved), (ii) the length of the wedge is greater than the length and width of the boulder, (iii) the shape is a closed form that is pointed at one end (i.e. the end extending away from the boulder), and (iv) the wedge has a ridge (which can be sharp or rounded) (Figure 28). In context, 'type B' wind-tail-like features are determined by (i) accumulated material does not spread out to form a wide elongated shape, (ii) the entire wind tail is not extended further, than by a factor of 1, of the height and width of the boulder, (iii) the wind tail morphology fades out away from the boulder (i.e. it becomes narrower, but there is no identifiable end point), and (iv) the wedge does not necessarily need to have a ridge (but may have one) (Figure 29). Those classified as type B, mostly occur on the 'head' lobe (Figure 33) as well as the 'back' of the 'body' lobe (Figure 35).

In generally, the most wind-tail-like features occur on the 'head' lobe of the comet. In the Ma'at region, the structures are observed at the boundaries of the large-scale depression region Hatmetit. In the Nut region, the wind-tail-like features mostly are located at the border to Ma'at. The Serqet region is subdivided into two distinct zones, each of which exhibits a prevalence of wind-tail-like features: Firstly, the southernmost zone which encompasses the region's tip and is extended to the area below the Nut region. Secondly, a zone located in the northern part of the Serqet region, situated on the periphery of the Nut region. On the 'body' lobe, the highest prevalence of wind-tail-like features is observed in the Ash region, and additionally in the Hapi 'neck' region (Figure 34). However, there are exceptions in the Seth region as well as in the Imhotep, Khepry and Aker regions (Figure 35). The prevailing direction of the wind-tail-like features on the northern hemisphere points roughly from south to north (Figure 34).

6 Discussion

The objective of this BSc thesis is to examine the phenomena of wind-tail-like features on comet 67P, in detail, after its perihelion. These post-perihelion results will be discussed separately in the Sections 6.1 to 6.3. As described in Section 5, a variety of wind-tail-like features on the surface of comet 67P could be observed. Their distribution on the comet will be discussed in Section 6.1. The wind-tail-like features have been sorted into types A and B, based on the classification scheme introduced in Section 4.2. These morphological types vary in terms of their occurrence, with type B being more common than type A. The precise reasons for this are unclear, but will be examined in Section 6.2. Furthermore, the orientation of the wind-tail-like features on the comet's nucleus will be discussed in Section 6.3.

Another study, investigating the pre-perihelion occurrence of wind-tail-like structures on comet 67P was undertaken by Sachse *et al.* (2022). The results of this work will be briefly presented in Section 6.4, in addition to a comparison with the post-perihelion results of this given BSc thesis. This pre- and post-perihelion comparison of wind-tail-like features on comet 67P is the first study of this type to be attempted, since it had not previously been conducted, prior to the research presented in this BSc thesis, and as such the results are new and not always easy to interpret.

6.1 Distribution of Wind-Tail-like Features

As noted above, the wind-tail-like features on comet 67P occur in two different morphological types. These structures, categorised into types A and B, are distributed unevenly across 67P's surface (Figure 33). However, the post-perihelion predominance of wind-tail-like features on the 'head' lobe suggests that the formation conditions for their genesis were more favourable there than on the 'body' lobe (Figure 34).

The hypotheses mentioned in Section 3.4, which try to explain the development of aeolian-like bedforms on the surface of comet 67P, are based on the process of cometary activity, which catapults material in the comet's coma by sublimation-driven out-

gassing. Thus, an exact length of material transport can not be determined, but generally the particles can be moved over much longer distances (compared to the aeolian and subaqueous transport known from the Earth) since the ejection removes them from the bedload entirely, bringing the particles also out of reach, where suspension could transport the grains. Resedimentation of these ejecta to the comet's surface happens by airfall processes, which leads to the deposition of NCM airfall layers on the surface of comet 67P.

In the period termed the post-perihelion, the wind-tail-like features predominantly occur in areas with NCM airfall deposits, supporting the proposed theory of Mottolla *et al.* (2015), which tries to explain their formation by the erosional process of abrasion of non-shielded areas of the comet's surface, so that the wind-tail-like features can form in protected zones, behind boulders acting as obstacles. As a consequence, it can be concluded that the formation of wind-tail-like features requires a dynamic environment, with the availability of impinging particles by airfall that pursue the process of abrasion.

The observation that large-scale areas in the regions termed Ash (on the 'body' lobe) and Ma'at (on the 'head' lobe), each located in high altitudes, do not present wind-tail-like features (Figure 34), although their presence could be expected since NCM airfall deposits are the dominant feature there (Table 1), also supports the assumption that a dynamic environment is key for the formation of wind-tail-like features on comet 67P. Thus, varied dynamic airfall conditions may also influence their deposition.

6.2 Morphological Types of Wind-Tail-like Features

As previously noted, two types of wind-tail-like features, A and B, based on the classification scheme of this BSc thesis (also see Section 4.2), were recorded from the comet's surface, in the observation period after comet 67P's perihelion transit. However, the controlling processes behind the two morphologies are not always clear, nor are they easy to determine.

Figure 37 shows that especially type B features are evident in the high-concentrated quadrant of the plot. This finding may hint that these smaller type B wind-tail-like features are in the process of being formed and are not yet as sufficiently developed as type A structures. However, looking at the Figures 33, 37 and 42, shows that this is not necessarily a general evolution and alternative explanations for the two morphological types, such as for example varied dynamic airfall conditions, could also contribute to the formation of different types of wind-tail-like features.

There are two reasons why the post-perihelion observation of the higher concentration of smaller wind tail-like features occurs: (i) The wind-tail-like features could have been newly formed in the time interval between the observation periods due to the available material from sublimation-driven outgassing after the comet's perihelion (also see Section 3.4). And (ii), the effect could also result from more detailed measurements due to better average image resolutions utilized (in comparison to previous studies, for this also see Section 6.4).

Addressing the formation of wind-tail-like features on comet 67P, it was proposed that the process is caused by surface abrasion and, thus, is categorised as an erosive procedure, rather than being depositional (Mottola *et al.* 2015). Based on the results of this present BSc thesis it would appear there are two perspectives on this. On the one hand, the erosional aspect of abrading the comet's surface that leads to the deposition of material in areas that are shielded by boulders, forming wind-tail-like features, seems plausible. This essentially is similar to processes also occurring elsewhere (e.g. on Earth, both in aeolian and subaqueous environments). But on the other hand, it could also be that, first, it is necessary for the impinging airfall particles to be deposited, i.e. attaining a particular thickness in building the layer of NCM airfall layers, which then, as described previously, can subsequently be eroded by surface abrasion. So one conclusion may be that the nature of the formation of wind-tail-like features on comet 67P could possibly be both depositional and erosional, meaning that particles are deposited first (in the form of NCM airfall layers), and, in addition, impinging airfall particles then build up the wedge of the wind-tail-like features by the erosional aspect of surface abrasion, which mobilizes material that deposits behind boulders act-

ing as obstacles, forming wide-spread elongated type A wind-tail-like features. This argumentation could then lead to the assumption that type B wind tail-like-structures, since they are not yet be as sufficiently developed as type A structures, are formed mostly by deposition due to airfall processes, with erosion by surface abrasion having a less important or direct influence. In contrast, this erosional process of surface abrasion may have played a more significant role in the formation of type A wind-tail-like features. Also, these processes may also have been influenced by further external factors, for example the surrounding topography, so that in some areas the active erosional process is more efficient than the deposition.

6.3 Orientations of Wind-Tail-like Features

As described in the results of this BSc thesis in Section 5, there are clear preferred orientations of the wind-tail-like features on the surface of comet 67P. Being consistent, the observed trend is from South to North. The precise reason for this marked orientation, however, is not always clear.

During the perihelion transit of 67P, the comet's southern hemisphere was directed towards the Sun. This resulted in elevated levels of cometary activity and a substantial rise in sublimation-driven outgassing on that particular side of the comet (Keller *et al.* 2017, Marshall *et al.* 2017). Outgassing resulted in significant erosion and mass loss (Gask *et al.* 2017). It can thus be assumed that the approximate South-to-North orientation of the wind-tail-like features, from the southern hemisphere (at the 'back' of the shape model) to the front side (Figure 34), indicates that the material originated from the southern hemisphere and was transported towards to the northern hemisphere in the wind-tail-like feature's directions. The result that more wind-tail-features were found, post-perihelion, in the mid latitudes supports this hypothesis (Figure 34).

6.4 Pre- and Post-Perihelion Comparison

A previous study, conducted by Sachse *et al.* (2022), also addressed wind-tail-like features on comet 67P albeit with one significant difference, their study focussed on the pre-perihelion situation. As part of this earlier study, 362 images were analysed, from which 41 were used to take measurements of boulders with wind-tail-like features. The images have an average resolution of 40.8 cm/pixel. In the observation period from October 2014 to February 2015, 39 wind-tail-like features were identified, which were not categorised into different types. The average boulder size is 15.9 m ± 6.7 m with a minimum of 4.6 m and a maximum of 35.5 m (Sachse *et al.* 2022). The wind-tail-like features are 15.2 m ± 9.9 m in length, with a minimum of 4.9 m and a maximum of 73.6 m (data comparison with post-perihelion in Table 3). Most features are less than 30 m in length (Figures 38 and 39).

	pre-perihelion	**post-perihelion**
boulder size	15.9 m ± 6.7 m	10.2 m ± 6.7 m
min	4.6 m	2.4 m
max	35.5 m	36.9 m
wind tail length	15.2 m ± 9.9 m	10.6 m ± 11.0 m
min	4.9 m	2.0 m
max	73.6 m	45.0 m
image resolution	40.7 cm/pixel	23.1 cm/pixel

Table 3: Data comparison table of the pre-perihelion results (Sachse *et al.* 2022) with the post-perihelion measurements (of this given BSc thesis), showing average values.

Comparing the linear slope fits of the analysed wind-tail-like features (Figures 38 and 39) for the pre-perihelion (0.94) and post-perihelion (1.04) datasets, it is clear that the overall data results of this BSc thesis can be considered valid, when compared to the pre-perihelion results published by Sachse *et al.* (2022) (Table 3). Although the measured values of the post-perihelion wind-tail-like features are generally lower than the pre-perihelion values published by Sachse *et al.* (2022), which probably is due to the better average image resolution of the post-perihelion images utilized (Table 3).

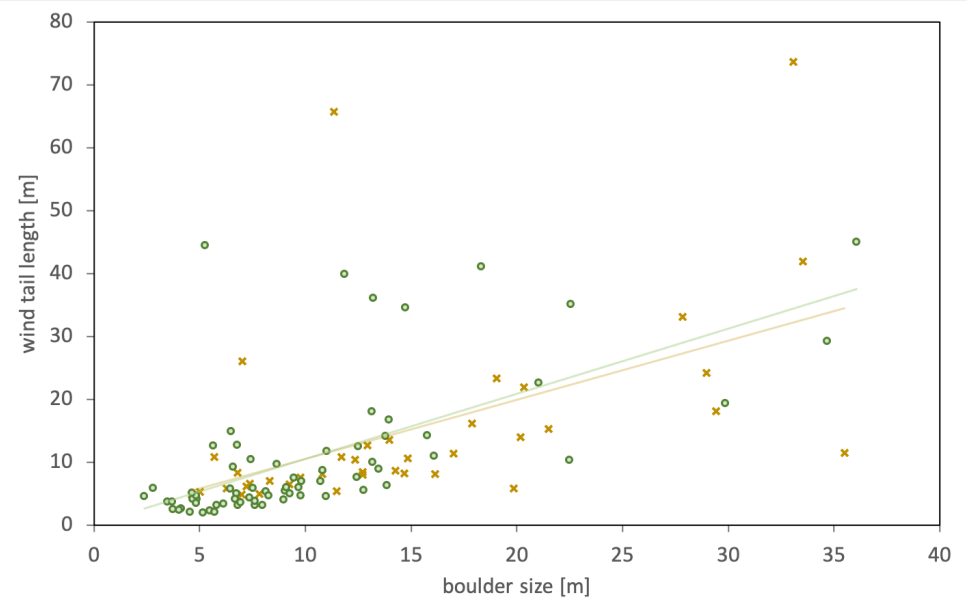

Figure 38: Plot of the boulder sizes (mean of the boulder's length and width) and the lengths of the wind-tail-like features. Pre-perihelion findings according to Sachse *et al.* (2022) (yellow), 39 features, slope fit 0.94. Post-perihelion results of this BSc thesis (green), 70 features, slope fit 1.04.

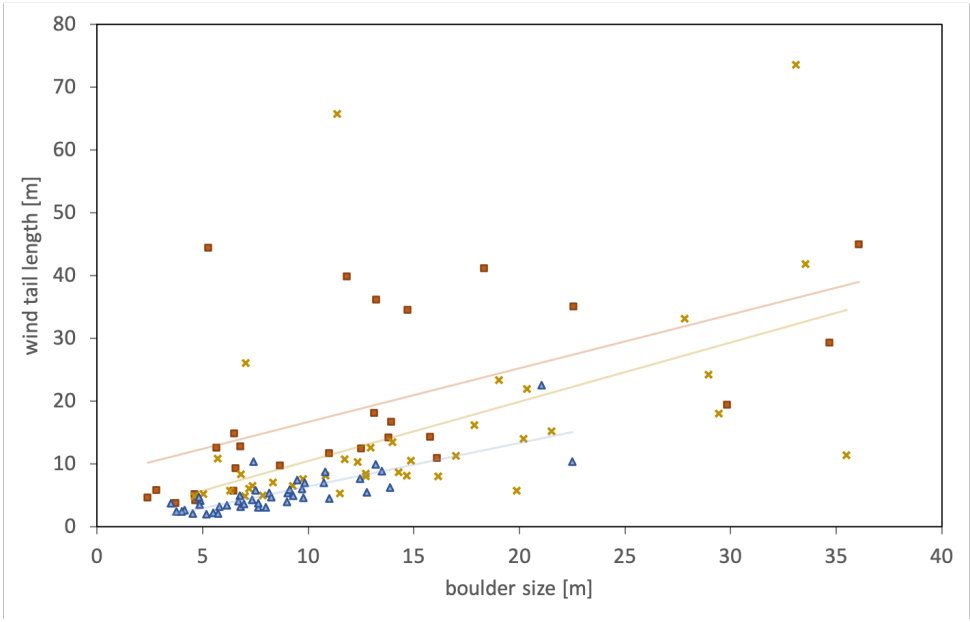

Figure 39: Plot of the boulder sizes (mean of the boulder's length and width) and the lengths of the wind-tail-like features. Pre-perihelion findings according to Sachse *et al.* (2022) (yellow), 39 features, slope fit 0.94. Post-perihelion, categorised in 27 type A (orange) and 43 type B (blue). Slope fits: 0.85 (type A), 0.69 (type B).

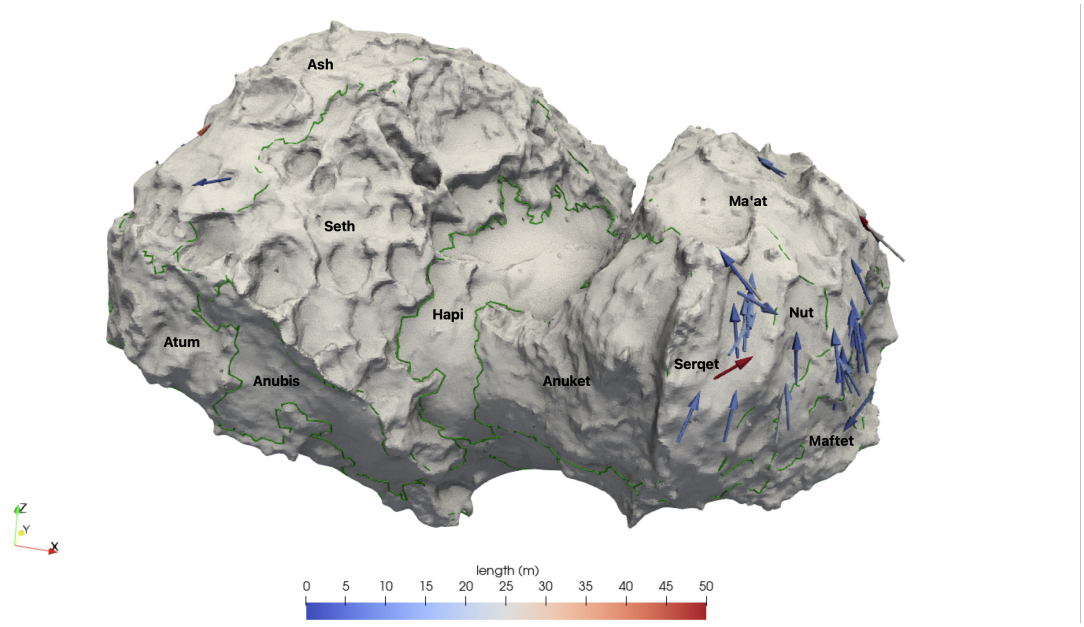

Figure 40: Pre-perihelion 3D overview map of the distribution and orientation of wind-tail-like features on the surface of the northern hemisphere of comet 67P ('front' view). Data from Sachse *et al.* (2022). The arrows are coloured according to their length. Green lines indicate the boundaries of geological regions.

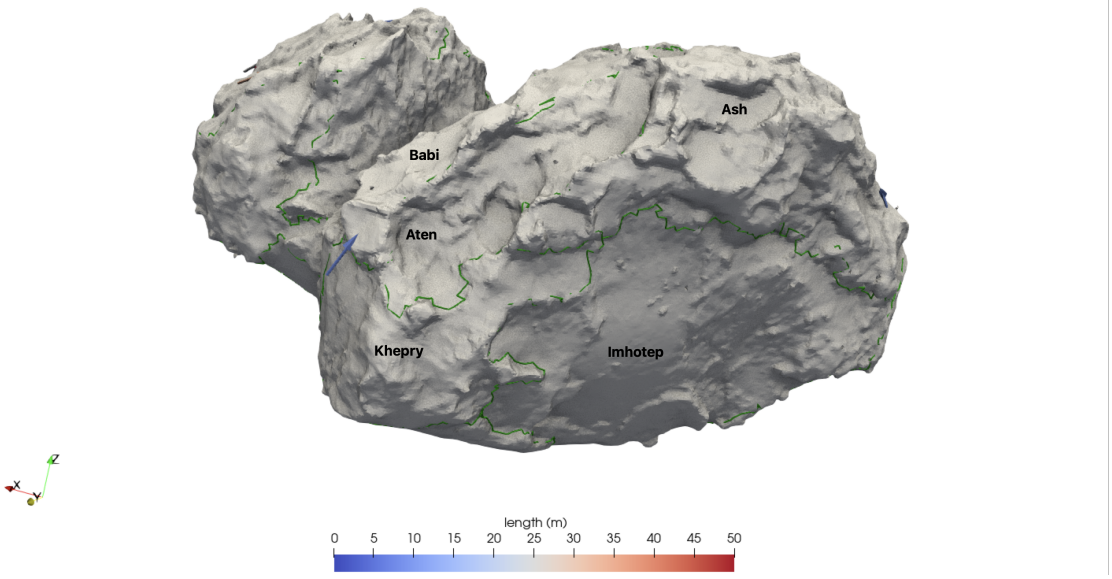

Figure 41: Pre-perihelion 3D overview map of the distribution and orientation of wind-tail-like features on the surface of the northern hemisphere of comet 67P ('back' view of the 'body' lobe). Data from Sachse *et al.* (2022). The arrows are coloured according to their length. Green lines indicate the boundaries of geological regions.

In comparison to the pre-perihelion results of Sachse *et al.* (2022), the post-perihelion images have better average image resolutions by a factor of 1.8 (Table 3). Both the pre-perihelion and post-perihelion measurements covered the entire (illuminated) surface of the comet (global approach). However, the enhanced resolution of the chosen post-perihelion images enabled a more comprehensive analysis of local details, thus, combining a global and local approach in this BSc thesis. The better image resolutions were also available for the study of Sachse *et al.* (2022) but were not necessarily considered based on their own image selection routine, balancing surface coverage and resolution.

Prior to perihelion, based on the results of Sachse *et al.* (2022), the majority of wind-tail-like features were observed on the 'head' lobe of the comet, particularly in the Ma'at and Serqet regions (Figure 40). Additionally, no features were observed in the 'neck' region (Figures 40). In contrast, only a limited number of features were identified on the 'body' lobe (Figure 40), and none were present on its 'back' (Figure 41).

Comparing the post-perihelion results of the distribution of wind-tail-like features on comet 67P of the given BSc thesis (Figures 34 and 35) with the pre-perihelion observations of Sachse *et al.* (2022) (Figures 40 and 41), the following findings, (i) to (iv), stand out particularly.

(i) Similar to the results of the given BSc thesis (also see Section 5), the pre-perihelion distribution of wind-tail-like features also occurs predominantly in areas with airfall NCM airfall deposits (Sachse *et al.* 2022).

(ii) In both the pre- and post-perihelion studies, the majority of wind-tail-like features were found on 67P's 'head' lobe. The hypothesis, previously described according to the post-perihelion findings of this BSc thesis, that the formation conditions for the genesis of wind-tail-like features on the 'head' lobe are more favourable than on the 'body' lobe is further supported by the observation that most observed wind-tail-like features were already present on the 'head' lobe prior to the comet's perihelion.

(iii) Wind-tail-like features in the Hapi 'neck' region were mapped only after the perihelion. The distinct post-perihelion findings of wind-tail-like features there, which were absent in the pre-perihelion study of Sachse *et al.* (2022), serves to provide further evidence that material transport during the active comet phase plays a significant role on the surface of comet 67P (Figure 42).

(iv) After the comet's perihelion, the distribution of wind-tail-like features has changed on the comet's 'body' lobe. In fact, post-perihelion, a greater number of wind-tail-like features could be identified on the comet's 'body' lobe, which are located in the Ma'at and Imhotep regions. The findings in the Ma'at region can be related to the presence of NCM deposits indicating dynamic airfall-like conditions. Although, the wind-tail-like feature's observations on the 'back' of the 'body' lobe, located in the Imhotep region (Figure 35), raise further questions, since it appears that gravitational processes such as mass wasting are of considerable importance for the region's geomorphological evolution (Auger *et al.* 2015). Figure 43 shows the findings in the Imhotep region, and gives possible examples of mass wasting deposits (labelled 1 to 3) and wind-tail-like features (labelled a to c). The mass wasting products are located 'before' the associated boulders, indicating in the direction down slope, and resulted due to the movement of material down the slope, and this motion being stopped by the obstacle (Figure 19). These, presumably, mass-wasting morphologies appear in more widespread widths, whereas wind-tail-like features result in forms that are elongated in length. Increased and more local as well as smaller-scale resolution analyses are required to verify the difference between mass wasting deposits and wind-tail-like features on comet 67P. Indeed, this could also be a reason as to why the structures were found only in the post-perihelion study of this given BSc thesis. Thus, in dedicated settings depending on the image resolution, mass wasting deposits can look similar to wind-tail-like features (Figure 43). A further description of these, possibly, morphological similarities of mass wasting deposits with wind-tail-like features on comet 67P is beyond the present image resolution limit.

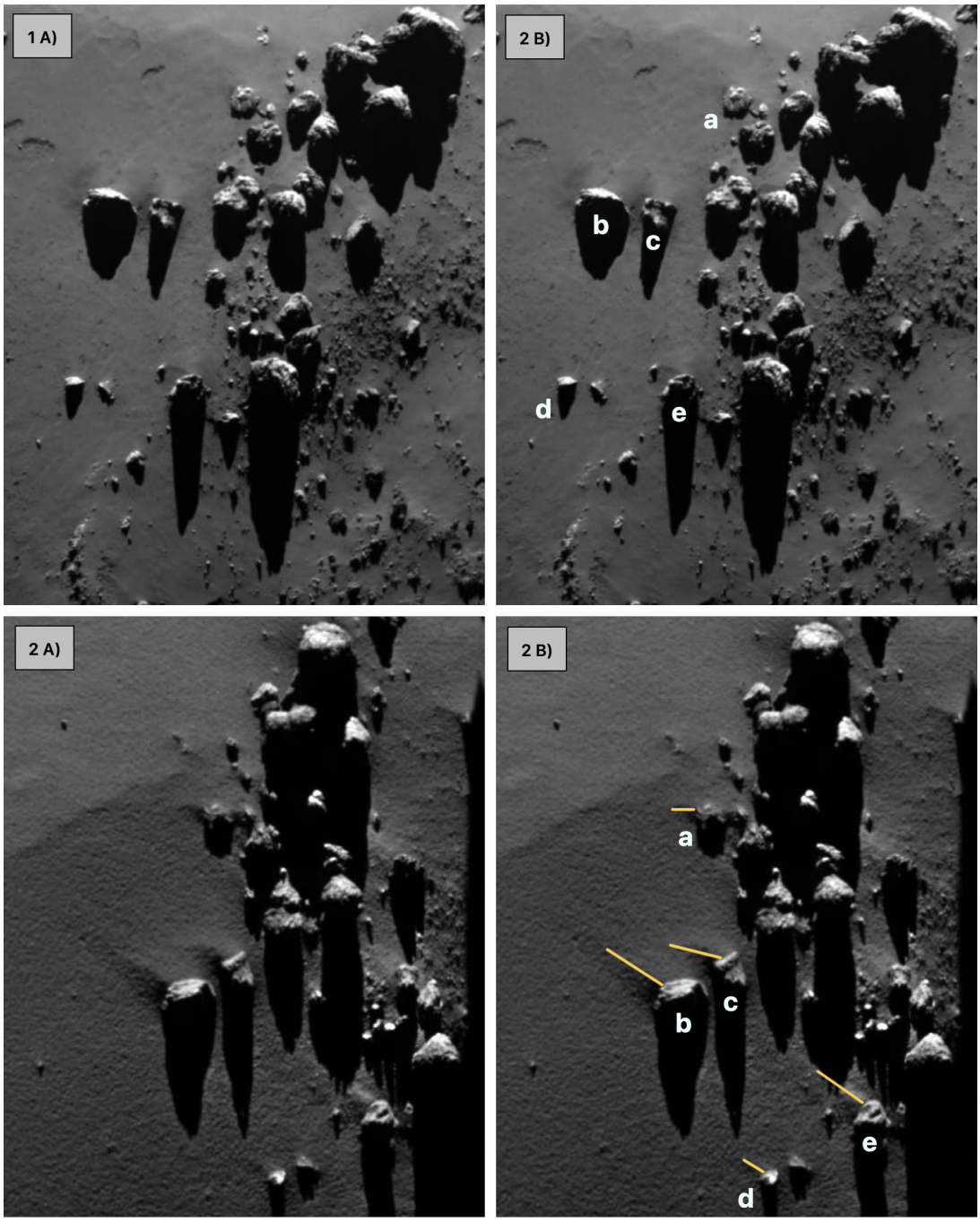

Figure 42: Comparison in the Hapi 'neck' region, small letters indicate the corresponding boulders. (Top): Pre-perihelion image from 22 January 2015. (Bottom): Post-perihelion measurements of this BSc thesis, image taken on 19 June 2016.

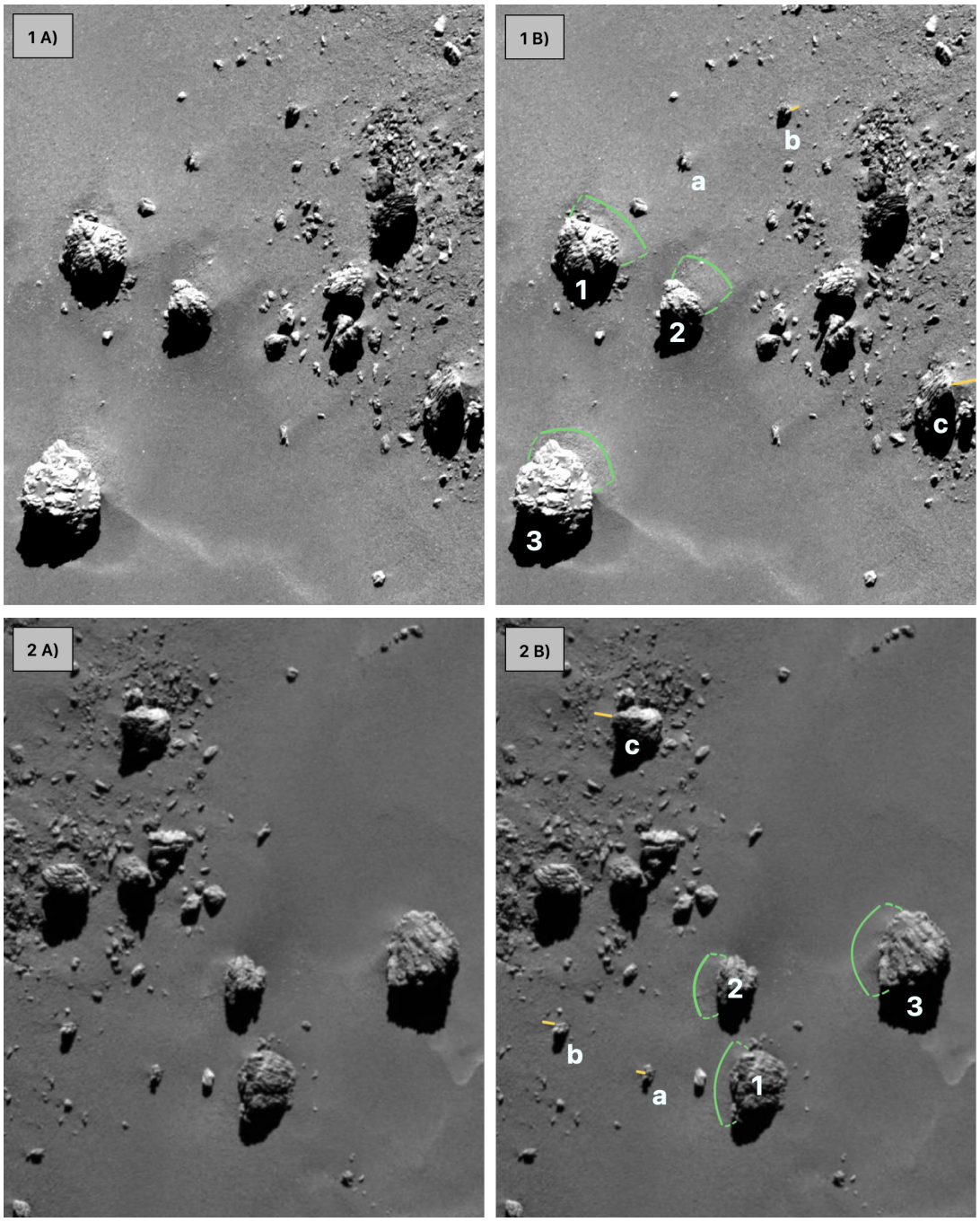

Figure 43: Comparison in the Imhotep region, on the 'back' of the 'body' lobe. The numbers as well as small letters indicate the corresponding boulders in the different images. 1-3 with green lines show possible mass wasting deposits 'before' boulders. The letters a-c with yellow lines indicate possible wind-tail-like features. In these images, all wind-tail-like features are categorised as type B. (Top): Pre-perihelion image from 14 February 2015. (Bottom): Post-perihelion measurements of this BSc thesis, image taken on 14 June 2016.

One other aspect is of particular interest. Two wind-tail-like features, both approximately 70 m in length, were noted in the pre-perihelion data, and neither of these could be identified in the post-perihelion study (Figure 38). This probably is due to the fact that these structures consist not of one, but of several cumulative wind-tail-like features, and as such, they are not single features.

In addition to the above, a final aspect is the subjectivity of the scientist working on the two studies, given that different people pursued the mapping. Also, it is important to note that the direct comparison of an individual wind-tail-like feature may be affected by different perspectives on the same area, which is particularly the case both for the pre- and post-perihelion data (Figure 44).

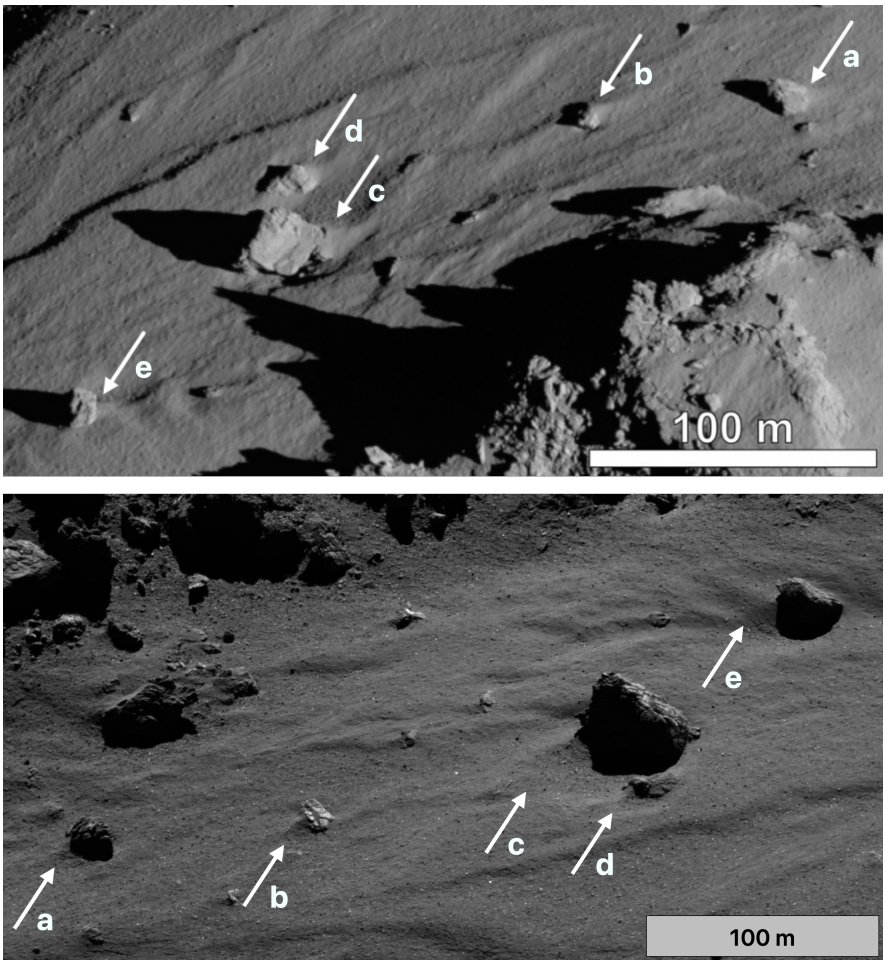

Figure 44: Example images of different perspectives on the same area, here within the Serqet region. (Top): Pre-perihelion (from Tirsch *et al.* 2017). (Bottom): Post-perihelion (this BSc thesis).

7 Conclusion

Aeolian wind tails are common on planets such as Earth and Mars (also see Section 1.1). Thus, the existence of aeolian-like beforms on comet 67P, including wind-tail-like features, is striking given the almost negligible gravity and absence of a traditional atmosphere in the cometary environment (also see Section 3.4).

Utilizing remote sensing images of comet 67P, which were taken by the OSIRIS Narrow Angle Camera (NAC) instrument onboard of the orbiter of ESA's Rosetta mission, in the observation period from 01 May to 31 July 2016, 1858 images were analysed searching for the post-perihelion occurance of wind-tail-like features on the comet's surface (also see Section 4). In 22 images, a total of 70 wind-tail-like features were found (also see Section 5), which were categorised in the morphological types A (27) and B (43), introduced in this given BSc thesis (also see Section 4.2). The geometric measurements of these wind-tail-like features on the highly irregularly shaped comet 67P were performed with the Small Body Mapping Tool (SBMT) from the Applied Physics Laboratory at John Hopkins University (Ernst *et al.* 2018), and are presented in a 3D overview map on 67P's shape model, which shows the distribution and orientation of the wind-tail-like structures on the surface (also see Section 5).

One highlight, with introducing the two morphological types of wind-tail-like features (also see Section 4.2), is concluding that, rather than being an erosive procedure (Mottola *et al.* 2015), the formation of wind-tail-like features on comet 67P could possibly be both depositional and erosional, with requiring a dynamic environment, where in some areas the active erosional process is more efficient than the deposition (also see Section 6.2).

All in all, it can be stated that this BSc thesis verified and deepened the scientific knowledge about wind-tail-like features on the surface of comet 67P. The comparison of pre- and post-perihelion of wind-tail-like structures on a comet had not previously been conducted, prior to the research presented in this given BSc thesis. Therefore, future studies are to be conducted to further address this research topic.

8 Acknowledgements

I would like to take this chance to thank all those who contributed to the completion of this thesis.

The opportunity to collaborate with the Institute of Planetary Research of the German Aerospace Centre (DLR) during my internship and the process of this thesis was instructive and exciting. My special gratitude goes to PD Dr. Katharina Otto for her exemplary personal supervision, invaluable guidance, and unwavering support throughout the course of my thesis.

I am also very grateful to Prof. Dr. Tom McCann from the University of Bonn for his scientific guidance and support.

Another particular acknowledgement goes to the team of the Small Body Mapping Tool (SBMT) from the Applied Physics Laboratory at John Hopkins University. Especially Dr. Carolyn Ernst, thank you for your support with my questions about the SBMT, and for providing the pointing files for the images I used. Your help was crucial in enabling me to successfully complete the data collection for my thesis.

9 References

Auger, A.-T., Groussin, O. *et al.* 2015. Geomorphology of the Imhotep region on comet 67P/Churyumov-Gerasimenko from OSIRIS observations. *Astronomy & Astrophysics*, **583**, https://doi.org/10.1051/0004-6361/201525947.

Barrington, M.N., Birch, S.P.D., Jindal, A., Hayes, A.G., Corlies, P. and Vincent, J.-B. 2023. Quantifying Morphological Changes and Sediment Transport Pathways on Comet 67P/Churyumov-Gerasimenko. *Journal of Geophysical Research: Planets*, **128**, https://doi.org/10.1029/2022JE007723.

Bennett, J.O., Donahue, M., Schneider, N. and Voit, M. (eds) 2020. *The Cosmic Perspective*, Pearson, London.

Capaccioni, F., Coradini, A. *et al.* 2015. The organic-rich surface of comet 67P/Churyumov-Gerasimenko as seen by VIRTIS/Rosetta. *Science*, **347**, https://doi.org/10.1126/science.aaa0628.

Deller, J. and Sierks, H. 2022. OSIRIS Optical, Spectroscopic, and Infrared Remote Imaging System OSIRIS Science User Guide. OSIRIS Image Archive, Max Planck Institute for Solar System Research, https://rosetta-osiris.eu/documents/SCIENCE_USER_GUIDE.

El-Maarry, M.R., Thomas, N. *et al.* 2015. Regional surface morphology of comet 67P/Churyumov-Gerasimenko from Rosetta/OSIRIS images. *Astronomy & Astrophysics*, **583**, https://doi.org/10.1051/0004-6361/201525723.

El-Maarry, M.R., Thomas, N. *et al.* 2016. Regional surface morphology of comet 67P/Churyumov-Gerasimenko from Rosetta/OSIRIS images: The southern hemisphere. *Astronomy & Astrophysics*, **593**, https://doi.org/10.1051/0004-6361/201628634.

El-Maarry, M.R., Groussin, O. *et al.* 2019. Surface Morphology of Comets and Associated Evolutionary Processes: A Review of Rosetta's Observations of 67P / Churyumov–Gerasimenko. *Space Science Reviews*, **215**, https://doi.org/10.1007/s11214-019-0602-1.

Ernst, C.M., Barnouin, O.S., Daly, R.T. and SBMT Team. 2018. The Small Body Mapping Tool (SBMT) for Accessing, Visualizing, and Analyzing Spacecraft Data in Three Dimensions. Paper LPI 2083, presented at the 49th Lunar and Planetary Science Conference, 19-23 March, The Woodlands, Texas.

ESA 2024. ESA's PSA FTP server. https://psaftp.esac.esa.int.

Gasc, S., Altwegg, K. *et al.* 2017. Change of outgassing pattern of 67P / Churyumov–Gerasimenko during the March 2016 equinox as seen by ROSINA. *Monthly Notices of the Royal Astronomical Society*, **469**, https://doi.org/10.1093/mnras/stx1412.

Keller, H.U., Mottola, S. *et al.* 2017. Seasonal mass transfer on the nucleus of comet 67P/ Chuyumov–Gerasimenko. *Monthly Notices of the Royal Astronomical Society*, **469**, https://doi.org/10.1093/mnras/stx1726.

Kofman, W., Herique, A. *et al.* 2015. Properties of the 67P/Churyumov-Gerasimenko interior revealed by CONSERT radar. *Science*, **349**, https://doi.org/10.1126/science.aab0639.

La Forgia, F., Giacomini, L. *et al.* 2015. Geomorphology and spectrophotometry of Philae's landing site on comet 67P/Churyumov-Gerasimenko. *Astronomy & Astrophysics*, **583**, https://doi.org/10.1051/0004-6361/201525983.

Jia, P., Andreotti, B. and Claudin, P. *et al.* 2017. Giant ripples on comet 67P / Churyumov–Gerasimenko sculpted by sunset thermal wind. *Proceedings of the National Academy of Sciences*, **114**, https://doi.org/10.1073/pnas.1612176114.

Jorda, L., Gaskell, R. *et al.* 2016. The global shape, density and rotation of Comet 67P/Churyumov-Gerasimenko from preperihelion Rosetta/OSIRIS observations. *Icarus*, **277**, https://doi.org/10.1016/j.icarus.2016.05.002.

Marshall, D.W., Hartogh, P. *et al.* 2017. Spatially resolved evolution of the local H_2O production rates of comet 67P/Churyumov-Gerasimenko from the MIRO instrument on Rosetta. *Astronomy & Astrophysics*, **603**, https://doi.org/10.1051/0004-6361/201730502.

Mottola, S., Arnold, G. *et al.* 2015. The structure of the regolith on 67P/Churyumov-Gerasimenko from ROLIS descent imaging. *Science*, **349**, https://doi.org/10.1126/science.aab0232.

Nichols, G. 2009. *Sedimentology and Stratigraphy.* Blackwell Science, London.

Otto, K.A., Tirsch, D. *et al.* 2017. Distribution and Orientation of Aeolian-like Windtails on comet 67P/Churyumov-Gerasimenko. Presented at the Asteroids, Comets, Meteors Conference, Montevideo, Uruguay.

Pajola, M., Vincent, J.-B. *et al.* 2015. Size-frequency distribution of boulders ≥ 7 m on comet 67P/Churyumov-Gerasimenko. *Astronomy & Astrophysics*, **583**, https://doi.org/10.1051/0004-6361/201525975.

Pätzold, M., Andert, T. *et al.* 2016. A homogeneous nucleus for comet 67P / Churyumov–Gerasimenko from its gravity field. *Nature*, **530**, https://doi.org/10.1038/nature16535.

Preusker, F., Scholten, F. *et al.* 2015. Shape model, reference system definition, and cartographic mapping standards for comet 67P/Churyumov-Gerasimenko - Stereophotogrammetric analysis of Rosetta/OSIRIS image data. *Astronomy and Astrophysics*, **583**, https://doi.org/10.1051/0004-6361/201526349.

Preusker, F., Scholten, F. *et al.* 2017. The global meter-level shape model of comet 67P / Churyumov-Gerasimenko. *Astronomy & Astrophysics*, **607**, https://doi.org/10.1051/0004-6361/201731798.

Röber, N. 2014. Paraview Tutorial for the Visualization of Earth- and Climate Science Data.

Rossi, A.P. and van Gasselt, S. (eds) 2018. *Planetary Geology*, Springer International Publishing, Cham, Switzerland, https://doi.org/10.1007/978-3-319-65179-8.

Sachse, M., Kappel, D., Tirsch, D. and Otto, K.A. 2022. Discrete Element Modeling of Aeolian-like Morphologies on Comet 67P/Churyumov-Gerasimenko. *Astronomy & Astrophysics*, **662**, https://doi.org/10.1051/0004-6361/202141296.

Sierks, H., Barbieri, C. *et al.* 2015. On the nucleus structure and activity of comet 67P/Churyumov-Gerasimenko. *Science*, **347**, https://doi.org/10.1126/science.aaa1044.

Taylor, M.G.G.T., Altobelli, N., Buratti, B.J. and Choukroun, M. 2017. The Rosetta mission orbiter science overview: the comet phase. *Philosophical Transactions of the Royal Society A: Mathematical, Physical and Engineering Sciences*, **375**, https://doi.org/10.1098/rsta.2016.0262.

Tirsch, D., Otto, K.A., Mottola, S., Hviid, S., Jaumann, R., Jorda, L. and Kührt, E. 2017. Tracing wind tails on 67P/Churyumov-Gerasimenko. Presented at the EPSC - European Planetary Science Congress.

Thomas, N., Sierks, H. *et al.* 2015a. The morphological diversity of comet 67P/Churyumov-Gerasimenko. *Science*, **347**, https://doi.org/10.1126/science.aaa0440.

Thomas, N., Davidsson, B. *et al.* 2015b. Redistribution of particles across the nucleus of comet 67P/Churyumov-Gerasimenko. *Astronomy & Astrophysics*, **583**, https://doi.org/10.1051/0004-6361/201526049.

Tubiana, C., Güttler, C. *et al.* 2015. Scientific assessment of the quality of OSIRIS images. *Astronomy & Astrophysics*, **583**, https://doi.org/10.1051/0004-6361/201525985.

Appendix

IMAGE	ALTITUDE [km]	RESOLUTION [cm/pixel]
N20160520T111606709ID4FF22	6.86	12.86
N20160605T165444694ID4FF22	25.88	48.53
N20160704T042348115ID4FF22	11.69	21.92
N20160720T105916336ID4FF22	8.80	16.50
N20160703T140348181ID4FF22	8.11	15.21
N20160703T195048186ID4FF22	8.55	16.03
N20160710T113836527ID4FF22	5.99	11.23
N20160710T130836518ID4FF22	7.60	14.25
N20160710T133836512ID4FF22	8.98	16.84
N20160710T135336541ID4FF22	8.90	16.69
N20160710T140836516ID4FF22	9.42	17.66
N20160619T110952748ID4FF22	29.61	55.52
N20160730T172632244ID4FF22	7.22	13.54
N20160522T090037679ID4FF22	7.01	13.14
N20160508T190716802ID4FF22	17.74	33.26
N20160515T211717029ID4FF22	8.63	16.18
N20160710T145336531ID4FF22	9.75	18.28
N20160720T080248392ID4FF22	7.91	14.83
N20160717T075919155ID4FF22	7.39	13.86
N20160614T172526772ID4FF22	27.36	51.30
N20160520T103608943ID4FF22	7.23	13.56
N20160617T112951605ID4FF22	30.08	56.40
AVERAGES	12.31	23.07

Table 4: Table of the images used for the measurements in the SBMT. ALTITUDE describes the spacecraft's distance to the comet's surface. For NAC-images: RESOLUTION = 0.00001875 * ALTITUDE.